Numerical investigation of the effect of defect population on the fatigue strength anisotropy of alloys fabricated by L-PBF

Sai Sreenivas Penkulinti, Nicolas Saintier, Matthieu Bonneric, Benoit Verquin, Thierry Palin-Luc, Fabien Lefebvre, Pascal Ghys

To cite this version:

Sai Sreenivas Penkulinti, Nicolas Saintier, Matthieu Bonneric, Benoit Verquin, Thierry Palin-Luc, et al.. Numerical investigation of the effect of defect population on the fatigue strength anisotropy of alloys fabricated by L-PBF. International Journal of Fatigue, 2026, 203, pp.109294. ⟨10.1016/j.ijfatigue.2025.109294⟩. ⟨hal-05328425⟩

HAL Id: hal-05328425
https://hal.science/hal-05328425v1

Submitted on 20 Nov 2025

International Journal of Fatigue 203 (2026) 109294

Contents lists available at ScienceDirect

International Journal of Fatigue

journal homepage: www.elsevier.com/locate/ijfatigue

Numerical investigation of the effect of defect population on the fatigue strength anisotropy of alloys fabricated by L-PBF

Sai Sreenivas Penkulinti [a,b], Nicolas Saintier [a,b,*], Matthieu Bonneric [a,b], Benoit Verquin [c], Thierry Palin-Luc [a,b], Fabien Lefebvre [d], Pascal Ghys [e]

[a] Univ. Bordeaux, CNRS, Bordeaux INP, I2M, UMR 5295, F-33400, Talence, France
[b] Arts et Metiers Institute of Technology, CNRS, Bordeaux INP, I2M, UMR 5295, F-33400 Talence, France
[c] CETIM, 7 Rue de la presse, Saint-Etienne, 42000, France
[d] CETIM, 52 Avenue Félix Louat, Senlis, 60300, France
[e] ALSTOM, 48 Rue Albert Dhalenne, Saint-Ouen-sur-Seine, 93400, France

ARTICLE INFO

Keywords:
Laser Powder Bed Fusion (L-PBF)
Defect
High-cycle fatigue
Finite element analysis
Statistics

ABSTRACT

This study investigates the impact of defects on the fatigue strength anisotropy of Ti-6Al-4V alloy fabricated by Laser Powder Bed Fusion (L-PBF). Finite element simulations are performed to analyze two defect populations, lack of fusion (LoF) defects and gas pores, under multiaxial proportional loading conditions. Results demonstrate that fatigue strength is highly sensitive to the polar angle θ representing the defect orientation with respect to the mechanical loading and is primarily influenced by defect morphology, transitioning from low sphericity (LoF defects) to high sphericity (gas pores). The anisotropic behavior is particularly pronounced under tensile loading, where the morphology of LoF defects and loading directions exhibit a notable influence. Shear loading exhibits reduced sensitivity to these factors. The proposed statistical methodology allow to determine the fatigue strength anisotropy for any multiaxial loading configuration and defect population. The numerically obtained fatigue strength anisotropy matches the one obtained experimentally in the literature and non-local analysis smoothens the fatigue strength surface response, leading to a reduction in the anisotropic factor (λ).

1. Introduction

The success of the Laser Powder Bed Fusion (L-PBF) process can be attributed to numerous factors, including the ability to tailor the microstructure by controlling the process parameters, which are known for their high flexibility. Additionally, L-PBF is recognized for its efficient material usage and ability to fabricate intricate industrial components with high dimensional accuracy [1]. Furthermore, L-PBF is considered as material-efficient technique due to its ability to recycle unused metal powder. However, it also presents key challenges, such as fabrication-induced defects (e.g., Lack of Fusion (LoF) defects and gas pores), which remain a major concern when designing industrial components susceptible to fatigue damage. The induced defects depend on the fabrication process. For instance, Lack of Fusion (LoF) defects arise due to insufficient energy input, leading to incomplete melting and poor fusion. Gas pores or voids trapped within the solidified material primarily result from pre-existing gases in the feedstock powder or the evaporation of volatile elements within the powder at high temperatures, making it difficult for the gases to escape as the melt pool solidifies [2,3].

Previous studies have shown that LoF defects notably reduce fatigue strength due to their tortuous morphology, which creates areas of high stress concentration [4–6]. In addition, fatigue strength is highly sensitive to several parameters within the defect population, such as defect size, shape, and location relative to the surface (surface, sub-surface, and internal) [7,8]. Furthermore, statistical analyses that consider the entire defect population characteristics such as the size distributions, defect densities, and spatial distributions are crucial for predicting the fatigue behavior [9]. Defect size is often acknowledged as the major factor impacting fatigue strength under uniaxial high-cycle fatigue (HCF) loading conditions [10–12]. According to Murakami and Endo [13], the fatigue limit of materials containing defects can be related to the defect size using the square root area (denoted as $\sqrt{\text{area}}$ in the following) parameter, which represents the projected area perpendicular to the maximum principal stress. They proposed a model based on Linear Elastic Fracture Mechanics (LEFM) to correlate

---

[*] Corresponding author at: Arts et Metiers Institute of Technology, CNRS, Bordeaux INP, I2M, UMR 5295, F-33400 Talence, France.
E-mail address: nicolas.saintier@ensam.eu (N. Saintier).

https://doi.org/10.1016/j.ijfatigue.2025.109294
Received 15 July 2025; Received in revised form 2 September 2025; Accepted 16 September 2025

Nomenclature

$\langle \mathrm{FIP} \rangle$	Fatigue Indicator Parameter averaged over a given volume
$\mathbf{d}$	Direction vector in spherical coordinates
$\mathbf{e}_\psi$	Azimuthal unit vector in spherical coordinates
$\mathbf{e}_\theta$	Polar unit vector in spherical coordinates
$\mathbf{e}_r$	Radial unit vector in spherical coordinates
$\mathbf{i}, \mathbf{j}, \mathbf{k}$	Cartesian unit vectors along x, y, z axes
$\mathbf{n}$	Normal vector in the Euclidean space $\mathbb{E}^3$
$\alpha,\ \beta$	Crossland criterion parameters
λ	Anisotropic factor of fatigue strength
ν	Poisson's ratio
ψ, θ, ϕ	Euler angles for rotation of stress tensors
Ψ	Sphericity
$\Sigma_{\mathrm{d}},\ \mathrm{T}_{\mathrm{d}},\ \underline{\underline{\Sigma}}^{(\mathrm{FS})}$	Numerical macroscopic fatigue strengths
$\Sigma_{\mathrm{d}_{-1}}$	Fully reversed fatigue strength in tension
$\Sigma_{\mathrm{h,max}}$	Maximum hydrostatic stress
$\sigma,\ \mu,\ \xi$	Gumbel distribution parameters
$\sqrt{J_{2,a}}$	Amplitude of 2nd invariant of the deviatoric local stress tensor
$\underline{\underline{\mathrm{T}}}^{(\mathrm{I})}$	Elementary stress tensors
d_{c}	Radius of the sphere over which stresses are averaged
$\mathrm{F}_{3\mathrm{d}}$	3D Feret diameter
$\mathrm{R}(\psi, \theta, \phi)$	Overall rotation matrix
$\mathrm{T}_{\mathrm{d}_{-1}}$	Fully reversed fatigue strength in torsion
V_{c}	Volume of sphere over which stresses are averaged
$\sqrt{\mathrm{area}}$	Murakami's defect size parameter
$\underline{\underline{s}}$	Deviatoric stress tensor
CT	Computed Tomography
DC	Danger coefficient
DVE	Defective Volume Element
E	Young's modulus
FE	Finite Element
FIP	Fatigue Indicator Parameter
GEV	Generalized Extreme Value
HCF	High-cycle Fatigue
HIP	Hot Isostatic Pressed
KDE	Kernel Density Estimation
LEFM	Linear Elastic Fracture Mechanics
LoF	Lack of Fusion
MPC	Multi-point Constraint
R	Stress ratio $\sigma_{\mathrm{min}}/\sigma_{\mathrm{max}}$

the fatigue strength to $\sqrt{\mathrm{area}}$, discriminating the internal and surface defect configurations. However this $\sqrt{\mathrm{area}}$ parameter is inapt to fully capture the criticality of defects with complex morphologies [14]. Additionally, depending on the defect's shape and the type of loading, the $\sqrt{\mathrm{area}}$ parameter may be difficult to define unambiguously. In uniaxial tensile loading the principal stress direction is unique, while for the torsional loading, for instance, the existence of two principal stress directions leads to two possibilities to define the $\sqrt{\mathrm{area}}$ parameter. Similarly, for non-proportional loadings, this parameter cannot be defined effectively.

In the HCF regime, surface and near-surface defects are known to be more harmful to fatigue behavior than internal defects, largely because of the significant influence of environmental conditions (such as vacuum, dry air, or ambient air) on the growth of fatigue cracks [15,16]. For the considered material, crack growth rates are lower in vacuum than in air condition. This is usually considered as the root cause of the higher criticality of surface defects as compared to internal defects since for the latter ones lower crack propagation rates result in higher fatigue lives [17–22]. In addition to environmental effects, the interaction between near-surface defects and the free surface leads to cyclic strain localization within the ligament (the ligament size between the free surface and the defect) [23], which promotes premature crack initiation compared to internal defects. Furthermore, elastic–plastic finite element simulations conducted by Z. Xu et al. [24] for ideal spherical defects revealed that the theoretical stress concentration factor (K_{t}) reaches its peak when the defect is in direct contact with the free surface. It should be noted that the environment may also modify the crack initiation (local plasticity to crack transition) phase but only very limited results exist in the literature on these aspects.

Studies focusing particularly on the impact of the defect morphology are also limited, and this defect feature is usually considered as a second order parameter contributing to the scatter of the fatigue resistance [25]. However, as shown in Léopold et al.'s work [26] for cast Ti64 alloy, local defect morphology may have a strong impact on the fatigue strength. A similar work on cast AlSi alloy revealed opposite trend with a limited impact of the local defect morphology on the fatigue strength [27]. These results suggest that the impact of the local defect morphology on the fatigue resistance depends on the material and possibly decreases when the ductility increases.

LoF defects are typically formed between the L-PBF layers due to insufficient fusion and often lead to anisotropic monotonic quasi-static tensile and fatigue properties. For instance, horizontally built samples (longitudinal axis perpendicular to the build direction (BD)) show higher fatigue strength than vertically built samples (longitudinal axis parallel to the build direction) [28,29]. This result is usually attributed to the fact that LoF defects in vertically built samples which are loaded parallel to the BD have a larger projected area than those in horizontally built samples [30–32]. Additionally, for multiaxial loadings, the orientation of the defects with respect to the loading directions might influence the fatigue behavior due to the morphological anisotropy of the defects. This impact of defect orientation is expected to be more significant with LoF defects, which have low sphericity compared to gas pores [33]. In a previous study on C45 structural steel by Z. Marciniak et al. [34], elliptical defects in the form of a one-sided notch were introduced at the surface of samples. These defects were placed at three different orientations (45°, 60°, and 90°) with respect to the main axis of the test specimens and subjected to fully reversed ($\mathrm{R} = -1$) bending and torsional loading conditions. Both experimental and numerical investigations revealed that defect orientation has a greater impact on the fatigue life under bending than under torsion, with 90°-oriented defects being more critical to fatigue behavior.

Nevertheless, the influence of defect orientation on multiaxial high-cycle fatigue strength has been little studied, particularly in the case of LoF defects, which are known for their complex morphology. To the best of the author's knowledge, there is no literature addressing this specific topic. Thus, in this study, a methodology is proposed to assess the impact of defects on the high-cycle fatigue strength anisotropy under multiaxial loadings, specifically for a high-strength material processed by L-PBF, using Finite Element (FE) simulations.

Several innovative aspects will be treated in this work, which can be summarized as follows. First, instead of considering ideal defect morphology configurations as in the majority of previous works dealing with multiaxial loadings, full field FE computation of real complex defect morphologies will be considered. Secondly, a statistical framework is proposed in order to address the fatigue strength anisotropy resulting from the combination of a complex defect population with multiaxial loadings that potentially cover all possible defect/loading misorientation. Third, considering the large number of computations

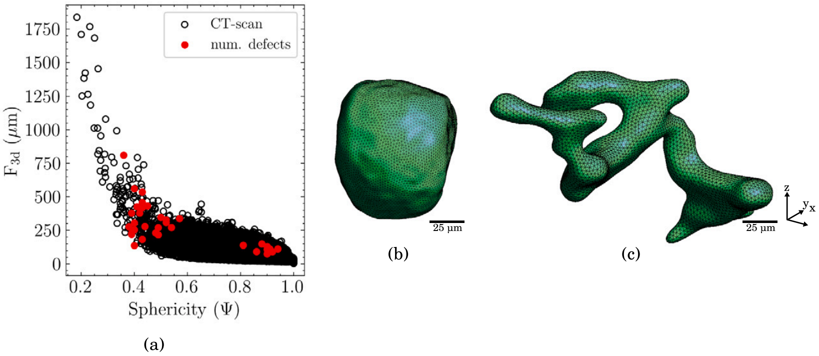

(a)

(b)

(c)

Fig. 1. (a) Feret diameter F_{3d} against sphericity, 3D views of meshed (a) gas pore and (b) LoF defect.

needed to cover all possible misorientation (around 390 000 computations per loading case (see Section 3 for more details)), an innovative reconstruction strategy is proposed to access the results at a low numerical cost. Fourth, a detailed methodology to efficiently visualize the resulting anisotropy is proposed. Finally a workflow that summarize the methodology to open the way of part positioning under fatigue properties constrain that include fatigue anisotropy properties will be presented.

2. Materials and methods

2.1. Material and defects

The alloy considered in this study is a Ti–6Al–4V, processed by L-PBF. The fatigue strengths at 10^6 cycles under fully reverse tension ($\Sigma_{d_{-1}} = 512$ MPa) and fully reversed torsion ($T_{d_{-1}} = 416$ MPa) were obtained in a previous work [35] for machined defect-free smooth samples. All the specimens were stress relieved and Hot Isostatic Pressed (HIP) prior testing to significantly reduce residual stresses and porosity. The aforementioned results will allow to determine the parameters of a multiaxial high-cycle fatigue strength criterion presented in the following sections.

Additional Ti–6Al–4V samples were processed by L-PBF using different sets of process parameters in order to generate controlled defect populations with distinct geometrical characteristics, gas pores and LoF defects (see Bonneric et al.'s study [36] for a detailed description). The resulting defect populations were characterized by micro-CT scans with a voxel size of 4 μm. Fig. 1a provides the distributions in size (expressed in terms of 3D Feret diameter F_{3d}) and sphericity Ψ of the defects for each population. Note that the Feret diameter is the maximum possible distance between the parallel planes that are tangent to opposite sides of the defect geometry, while the sphericity is given by Eq. (1) were V_p is the volume of the defect and A_p the surface area of the defect.

$$\Psi = \frac{\pi^{\frac{1}{3}} \left(6V_p\right)^{\frac{2}{3}}}{A_p} \tag{1}$$

25 LoF defects and 10 gas pores characterized by X-ray Computed Tomography (CT) are considered for the numerical simulations in the present study (the considered defects are highlighted in red in Fig. 1a). The selection of the LoF defect size range followed two criteria : i. the defect size corresponds to defects that are among the 5% largest defects in the population, ii. high defect density so that critical defects could be encountered in fatigue specimens. For the largest defects their density being relatively low, the probability of having such a defect in experimental test would be low due to scale effect. For further details on the scale effect, please refer to [16]. Fig. 1b and c provides 3D views of typical gas pore and LoF defect that have been used for finite element simulations. The number of defects to be chosen for numerical modeling was based on the adequate balance between stabilization of the statistical parameters describing the FIP distribution (presented in the following) and the numerical cost of adding new defects. It was considered that a sufficient number of defects were chosen when the variation of the GEV distribution function parameters was less than 1% when adding more defects to the analyses, geometry of the gas pores exhibiting less variability than that of the LoF defects (see the ranges of the sphericities and sizes values in Fig. 1 for example), 10 gas pores were found to be sufficient to capture the scatter of fatigue behavior induced by variations in the gas pore geometry from one defect to another. The proposed methodology focuses on the capture of the effect of local stresses due to the combination of complex defect morphologies and complex multiaxial loadings. Heterogeneous stress fields resulting from local heterogeneity at the grain scale are not considered here but were considered on ideal defects in a previous study by Guerchais et al. [37].

2.2. Meshing and calculation

For each selected defect, a surface mesh is performed using the Avizo® software. The defect is then positioned at the center of a cubic volume whose length is 5 times the size of the defect, before meshing the volume with quadratic tetragonal elements with GMSH software, as illustrated in Fig. 2a. In the following the cube containing the defect will be denoted Defective Volume Element (DVE). The total number of elements in the each DVE is around 10^6, with an element size at the vicinity of the defect of approximately 2.5 μm. Multi-point Constraint (MPC) periodic boundary conditions are used to prescribe the cyclic loading applied to the cube. Three different loading conditions are considered in this study (see Fig. 2b), all corresponding to a loading ratio of $R = -1$, which are (a) fully reverse tension ($\Sigma_{a,0}$), (b) fully reverse shear ($T_{a,0}$), and (c) in-phase combined tension–shear stress with a biaxial stress ratio of $T_{a,0} / \Sigma_{a,0} = 1$. In addition for each loading case, all the possible loading directions with respect to the defects will be considered. The exact methodology is described in Section 3. The material behavior is assumed to be linear elastic isotropic with a Young's modulus $E = 110$ GPa and Poisson's ratio $\nu = 0.34$. All finite element calculations have been performed using the FE code Z-set.

2.3. Post-processing — Application of a multiaxial HCF criterion

In order to simulate whether the applied loading would initiate a fatigue crack at 10^6 cycles, a multiaxial HCF strength criterion is used as a post-processing procedure on the FEA results on each considered couple (defect/loading condition). For ease of implementation in the FE tools. The Crossland criterion [38] is used, where the Crossland Fatigue Indicator Parameter (FIP), Eq. (2), is a linear combination of the amplitude of the 2nd invariant of the deviatoric stress tensor $J_{2,a}$ and the maximum hydrostatic stress $\Sigma_{h,max}$, as expressed in Eq. (2):

$$\text{FIP} = \sqrt{J_{2,a}} + \alpha \cdot \Sigma_{\text{h,max}} \tag{2}$$

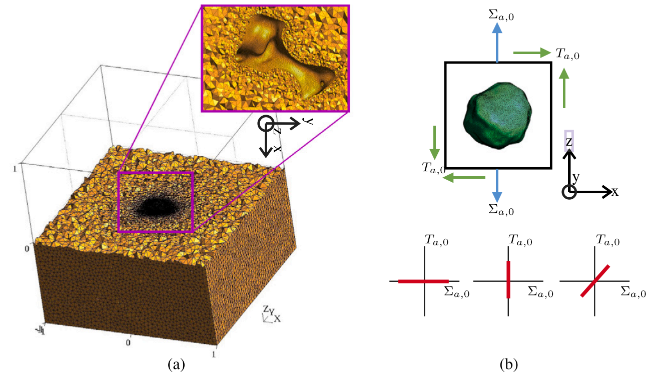

Fig. 2. Schematic illustration of the numerical study methodology, (a) mesh generation, and (b) multi-axial fatigue loading conditions.

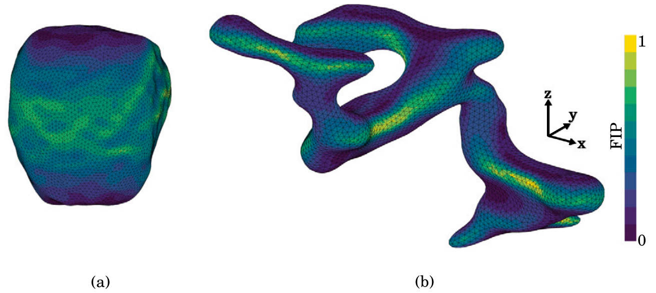

Fig. 3. FIP distribution on the surface of (a) gas pore and (b) LoF defect. (Note: FIPs are normalized for this illustration).

The calculation of $J_{2,a}$ is obtained by a double maximization over a loading period [10] as expressed in Eq. (3), where $\underline{\underline{s}}$ is the deviatoric part of the stress tensor. $\Sigma_{h,max}$ is given by Eq. (4). At each point, for a given cyclic loading condition the fatigue strength at 10^6 cycles is reached when the following condition is reached when $\sqrt{J_{2,a}} + \alpha \cdot \Sigma_{h,max} = \beta$. The criterion parameters α and β have been identified from the experimental fatigue strengths at 10^6 cycles $\Sigma_{d_{-1}}$ and $T_{d_{-1}}$ corresponding to uniaxial tension loading (R = −1) and torsion loading (R = −1), respectively [35].

$$\sqrt{J_{2,a}} = \frac{1}{2\sqrt{2}} \max_{t_i \in T} \left\{ \max_{t_j \in T} \sqrt{\left(\underline{\underline{s}}(t_i) - \underline{\underline{s}}(t_j)\right) : \left(\underline{\underline{s}}(t_i) - \underline{\underline{s}}(t_j)\right)} \right\} \tag{3}$$

$$\Sigma_{h,max} = \frac{1}{3} \max_{t \in T} \left(\mathrm{tr}(\underline{\underline{\Sigma}}(t)) \right) \tag{4}$$

In the post-processing step, the FIP distributions on the surface of the defects (see Fig. 3) are considered to determine the maximum FIP value designated as FIP_{max}. A fatigue crack is considered to initiate when the condition $FIP_{max} \geq \beta$ is fulfilled in the DVE. The macroscopic load leading to $FIP_{max} = \beta$ will therefore be designated as the numerical macroscopic fatigue strength, and noted Σ_d under fully reversed uniaxial loading (or T_d for the shear case). Since the material behavior is considered as linear elastic, there is a linear relation between the applied macroscopic loading and the local stress state. For this reason, it is possible to evaluate the numerical macroscopic fatigue strengths from a single computation under an arbitrary applied macroscopic stress level. Indeed, if under a prescribed macroscopic loading Σ_a the maximum FIP value is FIP_{max,Σ_a}, the numerical fatigue strength Σ_d is given by :

$$\Sigma_d = \frac{\Sigma_a}{FIP_{max,\Sigma_a}} \beta \tag{5}$$

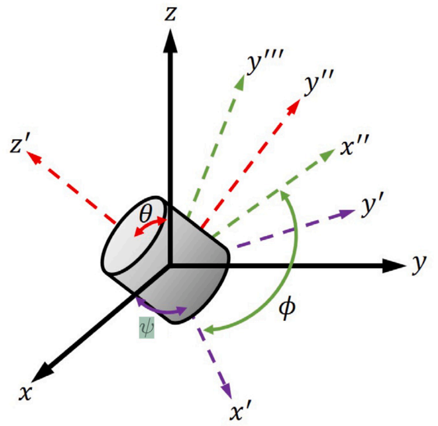

Fig. 4. Illustration showing three consecutive rotations used to transform a stress tensor. These include (i) first rotation around z-axis at an angle ψ, (ii) second rotation around x'-axis at an angle θ, (iii) third rotation around z'-axis at an angle ϕ.

The post-processing procedure described previously corresponds to a local analysis of the stress field since the FIP field is computed from the stress state at each node of the mesh. Several authors have shown that local analyses lead to conservative predictions of fatigue strength [39–41], and it is important to account for the stress/strain gradients surrounding stress raisers to accurately simulate the HCF strength. To do so, a non-local Fatigue Indicator Parameter ⟨FIP⟩ is introduced. It corresponds to the volume averaging of the local FIP over a small volume V_c [42,43] (see Eq. (6)). This volume corresponds to the part of material included in a sphere of radius d_c centered at the hotspot. A d_c value of 6 μm is considered for the studied material based on a previous work [44]. It also has to be noted that the averaging volume is truncated near the surface of the defect.

$$\langle FIP \rangle = \frac{1}{V_c} \iiint_{V_c} FIP \, dV \tag{6}$$

3. Numerical methodology to assess the HCF strength anisotropy

As stated in the introduction section the target of this work is to cover all possible misorientations between the defect population and the applied multiaxial loading. As an example, for a single defect under tensile loading, varying the orientation in 15° increments results in 625 computations, and for all 25 LoF defects considered, this totals 15,625 computations. In shear loading, including a third rotational angle (see below for more detail about that third rotation), the total number of computations for all 25 defects exceeds 390,000. To limit the numerical cost of such extensive computation cases, an efficient reconstruction strategy is detailed in the following.

In order to evaluate the defect orientation effect on the identified numerical HCF strength, two ways are possible. Either rotate the defect and fix the loading orientation, or rotate the loading and fix the defect orientation. The latter has the advantage of not having to remesh the considered volume element for each new configuration and to only manipulate the applied macroscopic stress tensor. If we consider an arbitrary applied macroscopic stress tensor $\underline{\underline{\Sigma}}$ on the DVE, its rotation from a reference basis to a new rotated basis is performed utilizing the Bunge Euler angle convention [45] (see Fig. 4) by applying three subsequent rotations as described in Eq. (7):

$$(x, y, z) \xrightarrow[\psi]{z \text{ axis}} (x', y', z) \xrightarrow[\theta]{x \text{ axis}} (x', y'', z') \xrightarrow[\phi]{z \text{ axis}} (x'', y''', z') \tag{7}$$

As shown in Fig. 4, ψ represents the azimuthal angle, corresponding to the rotation about the z-axis. θ is the polar angle, associated with the rotation about the x'-axis. Finally, ϕ, often referred to as the spin angle, corresponds to the third rotation about the z'-axis. This rotation sequence is consistent across all the loading types considered. To achieve a uniform distribution of data points across the 3D space that describes the overall rotation and ensure accurate quantification of fatigue strength anisotropy, the angles ψ, θ, and ϕ were discretized from 0° to 360° in increments of 15°. The rotation matrices corresponding to each rotation are provided in Eq. (8), while the overall rotation matrix R corresponds to Eq. (9).

$$
\begin{aligned}
R_z(\psi) &= \begin{bmatrix} \cos\psi & \sin\psi & 0 \\ -\sin\psi & \cos\psi & 0 \\ 0 & 0 & 1 \end{bmatrix}, \quad \psi \in [0, 2\pi] \\
R_x(\theta) &= \begin{bmatrix} 1 & 0 & 0 \\ 0 & \cos\theta & \sin\theta \\ 0 & -\sin\theta & \cos\theta \end{bmatrix}, \quad \theta \in [0, \pi] \\
R_z(\phi) &= \begin{bmatrix} \cos\phi & \sin\phi & 0 \\ -\sin\phi & \cos\phi & 0 \\ 0 & 0 & 1 \end{bmatrix}, \quad \phi \in [0, 2\pi]
\end{aligned} \tag{8}
$$

$$
\mathrm{R}(\psi, \theta, \phi) = \mathrm{R}_z(\phi)\mathrm{R}_x(\theta)\mathrm{R}_z(\psi) \tag{9}
$$

The rotated macroscopic stress tensor $\underline{\underline{\Sigma}}'(\mathrm{t})$ is then computed as follows:

$$
\underline{\underline{\Sigma}}'(\mathrm{t}) = \mathrm{R}\ \underline{\underline{\Sigma}}(\mathrm{t})\ \mathrm{R}^{\mathrm{T}} \tag{10}
$$

This rotated tensor $\underline{\underline{\Sigma}}'(\mathrm{t})$ can be written as a linear function of 6 independent elementary macroscopic stress tensors (see Eq. (11)), which are designated as $\underline{\underline{\mathrm{T}}}^{\mathrm{k}}(\mathrm{t})$ in what follows, where k is an index corresponding to the Voigt notation. The expressions of these 6 elementary tensors are provided in Eq. (12).

$$
\underline{\underline{\Sigma}}'(\mathrm{t}) = \sum_{\mathrm{k}=1}^{6} \Sigma'_{\mathrm{k}}(\mathrm{t})\ \underline{\underline{\mathrm{T}}}^{\mathrm{k}} \tag{11}
$$

$$
\begin{array}{ll}
\underline{\underline{T}}^1 = \begin{bmatrix} 1 & 0 & 0 \\ 0 & 0 & 0 \\ 0 & 0 & 0 \end{bmatrix} & \underline{\underline{T}}^2 = \begin{bmatrix} 0 & 0 & 0 \\ 0 & 1 & 0 \\ 0 & 0 & 0 \end{bmatrix} \\
\quad = e_1 \otimes e_1 & \quad = e_2 \otimes e_2 \\[2ex]
\underline{\underline{T}}^3 = \begin{bmatrix} 0 & 0 & 0 \\ 0 & 0 & 0 \\ 0 & 0 & 1 \end{bmatrix} & \underline{\underline{T}}^4 = \begin{bmatrix} 0 & 0 & 0 \\ 0 & 0 & 1 \\ 0 & 1 & 0 \end{bmatrix} \\
\quad = e_3 \otimes e_3 & \quad = e_3 \otimes e_2 + e_2 \otimes e_3 \\[2ex]
\underline{\underline{T}}^5 = \begin{bmatrix} 0 & 0 & 1 \\ 0 & 0 & 0 \\ 1 & 0 & 0 \end{bmatrix} & \underline{\underline{T}}^6 = \begin{bmatrix} 0 & 1 & 0 \\ 1 & 0 & 0 \\ 0 & 0 & 0 \end{bmatrix} \\
= e_1 \otimes e_3 + e_3 \otimes e_1 & = e_1 \otimes e_2 + e_2 \otimes e_1
\end{array} \tag{12}
$$

For each macroscopic stress tensors $\underline{\underline{\mathrm{T}}}^{\mathrm{k}}$, it is possible to compute the associated stress field $\underline{\underline{\mathrm{t}}}^{\mathrm{k}}(\underline{\mathrm{x}})$ in the DVE containing a given defect. The problem being fully linear, the stress field in the DVE $\underline{\underline{\sigma}}'(\underline{\mathrm{x}})$ corresponding to the rotated loading can be obtained from the 6 stress fields $\underline{\underline{\mathrm{t}}}^{\mathrm{k}}(\underline{\mathrm{x}})$ associated to the aforementioned elementary tensors by using the superposition principle (Eq. (13)).

$$
\underline{\underline{\sigma}}'(\underline{\mathrm{x}}, \mathrm{t}) = \sum_{\mathrm{k}=1}^{6} \Sigma'_{k}(\mathrm{t})\ \underline{\underline{\mathrm{t}}}^{\mathrm{k}}(\underline{\mathrm{x}}) \tag{13}
$$

Thus, the finite element computations of the stress field $\underline{\underline{\mathrm{t}}}^{\mathrm{k}}(\underline{\mathrm{x}})$ on each DVE for the 6 elementary loading tensors allow to assess the stress field, corresponding to any rotated loading knowing $\underline{\underline{\Sigma}}(\mathrm{t})$ and the Euler rotation angles ψ, θ and ϕ.

This procedure can be applied for any loading conditions, in the present case tension, shear and combined tension–shear, whose initial macroscopic stress tensors are:

$$
\begin{aligned}
\underline{\underline{\Sigma}}(\mathrm{t})_{\mathrm{tension}} &= \begin{bmatrix} 0 & 0 & 0 \\ 0 & 0 & 0 \\ 0 & 0 & \Sigma_{\mathrm{zz}}(\mathrm{t}) \end{bmatrix} \\
\underline{\underline{\Sigma}}(\mathrm{t})_{\mathrm{shear}} &= \begin{bmatrix} 0 & 0 & \Sigma_{\mathrm{xz}}(\mathrm{t}) \\ 0 & 0 & 0 \\ \Sigma_{\mathrm{zx}}(t) & 0 & 0 \end{bmatrix} \\
\underline{\underline{\Sigma}}(\mathrm{t})_{\mathrm{combined}} &= \begin{bmatrix} 0 & 0 & \Sigma_{\mathrm{xz}}(t) \\ 0 & 0 & 0 \\ \Sigma_{\mathrm{zx}}(t) & 0 & \Sigma_{\mathrm{zz}}(t) \end{bmatrix}
\end{aligned} \tag{14}
$$

The numerical reconstruction procedure was validated by comparing the superposed stress fields with direct finite element simulations with a difference of less than 0.01%. Following the assembly of the final stress state, danger coefficient (DC), DC $= \frac{\mathrm{FIP}_{\mathrm{max}}}{\beta}$ values are determined for each combination of Euler angles. Subsequently, macroscopic numerical fatigue strengths are identified from these values. Specifically, the value of the macroscopic loading corresponding to the fatigue strength $\underline{\underline{\Sigma}}^{\mathrm{FS}}$ is obtained as $\underline{\underline{\Sigma}}^{\mathrm{FS}}(\mathrm{t}) = \underline{\underline{\Sigma}}(\mathrm{t})/\mathrm{DC}$. The numerical reconstruction procedure was validated by comparing the superposed stress fields with direct finite element simulations, and, as expected a perfect match was obtained.

In the case of pure tension, the final rotation corresponding to the ϕ angle does not affect the final applied loading. In that particular loading case, the loading direction aligns with the final rotation axis z' (see Fig. 4). Consequently, for this specific loading case, the rotated loading direction can be fully described by the ψ and θ angles. This enables the results to be visualized as a function of the loading directions using a spherical plot or surface response plot (as described in J. Nordmann et al.'s study on elastic anisotropy [46]) involving spherical coordinates as illustrated in Fig. 5b.

The vector **d**, which corresponds to the loading direction for which the fatigue strength is being evaluated, is expressed as follows in spherical coordinates:

$$
\mathbf{d} = \begin{pmatrix} \sin(\theta)\cos(\psi) \\ \sin(\theta)\sin(\psi) \\ \cos(\theta) \end{pmatrix}_{\mathrm{i,\ j,\ k}} \tag{15}
$$

The sphere shown in Fig. 5b therefore represents all the possible loading directions, with the ψ angle varying between 0 and 2π, and the θ angle varying between 0 and π. In the present work, this sphere has been discretized considering specific combinations of ψ and θ angles with an increment size of 15° between consecutive angles, indicated by the black dots in Fig. 5b. For a given loading direction, the corresponding fatigue strength Σ_{d} is reported on the spherical plot with the coordinate point $\Sigma_{\mathrm{d}} \cdot \mathbf{d}$. The set of all these points forms a 3D surface, an example of which is provided in Fig. 6, with deviations from the ideal spherical shape indicating the level of anisotropy.

It is noteworthy that the third rotation angle ϕ has an impact on the final rotated loading for the cases of shear and combined tension–shear loading conditions, meaning that each direction **d** on the spherical plot is related to several fatigue strengths corresponding to the variations in the ϕ angle. This point will be addressed in Section 4.3.1.

4. Results and discussions

4.1. LoF defects loaded in tension

4.1.1. Local analysis

The statistical workflow for analyzing fatigue strength anisotropy is illustrated in Fig. 7a–d. Considering a pure macroscopic tensile stress, the surface responses were determined for the 25 considered LoF defects (see Fig. 7a and b), using the fatigue strengths determined from a local analysis as detailed in Section 3. In each direction $\mathbf{d}(\psi, \theta)$, Generalized Extreme Value (GEV) statistics were applied to the fatigue

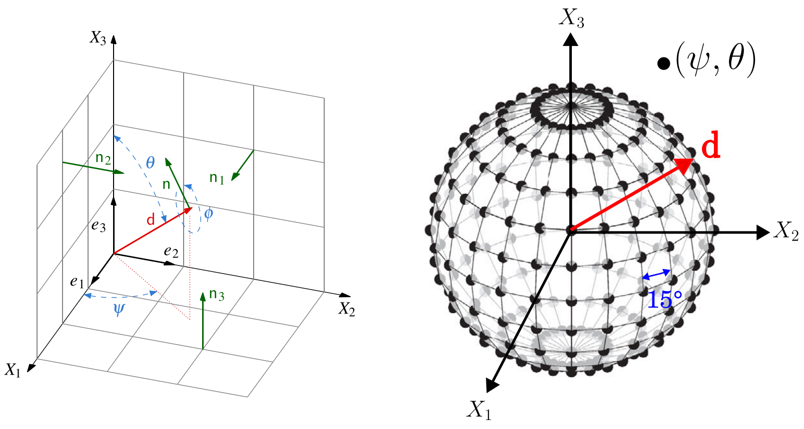

(a) (b)

Fig. 5. (a) Parameterization of the loading direction **d** with the Euler angles (image extracted from [46]) (b) Representation of the loading direction **d** using spherical coordinates (spherical plot) The black dots correspond to the loading directions considered in the present study. In reference to Fig. 4 X_1 is x-axis, X_2 is y-axis and X_3 is z-axis.

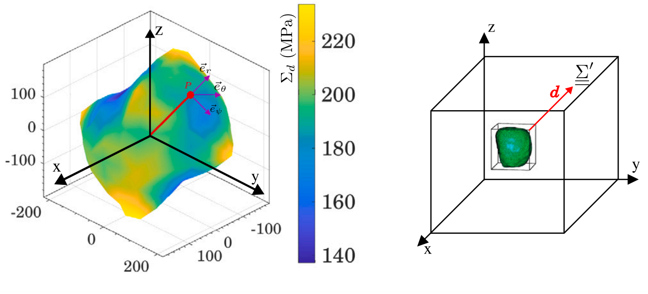

(a) (b)

Fig. 6. (a) Spherical plot of a defect (gas pore), (b) Illustration of the loading direction in red corresponding to the point P on the surface response.

strengths of all the 25 defects to identify the distribution parameters (Fig. 7c). Finally, the derived parameters enabled us to obtain a median surface response (Fig. 7d), quantifying the HCF strength anisotropy.

The Generalized Extreme Value (GEV) statistics is a powerful tool for capturing the statistical tendency of the extreme (weakest) values within a dataset. Murakami and coauthors [7,47] were the first to apply extreme value theory to estimate the maximum inclusion size in a large volume of steel, based on data sets from smaller volumes. The GEV cumulative distribution function is given by:

$$F(x)=\begin{cases}\exp\left(-\left(1+\xi\left(\frac{x-\mu}{\sigma}\right)\right)^{-\frac{1}{\xi}}\right), & \text{if } \xi\neq 0\\ \exp\left(-\exp\left(-\frac{x-\mu}{\sigma}\right)\right), & \text{if } \xi=0\end{cases} \tag{16}$$

where μ is the location parameter, $\sigma > 0$ is the scale parameter and ξ is the shape parameter. ξ determines the type of extreme value distribution: $\xi > 0$ indicates a Fréchet distribution, $\xi < 0$ corresponds to a Weibull distribution and $\xi = 0$ indicates a Gumbel distribution.

4.1.2. Extreme value statistics — analysis

As mentioned earlier, for each 25 LoF defects, the fatigue strength for a given loading direction (ψ,θ) is extracted in order to build the distribution and determine the associated GEV parameters. To identify the most suitable extreme value distribution for the numerical data, a contour plot of the shape parameter ξ is plotted for various combinations of loading directions (ψ,θ) for LoF defects, as shown in Fig. 8. Due to the symmetry of the spherical plot, the range of ψ and θ is limited to 0 to 180°. From this contour plot, it is observed that most values of ξ in the GEV distribution are close to zero, indicating that the data is best represented by a Gumbel distribution ($\xi = 0$). Therefore, the numerical results discussed in this study are analyzed using a Gumbel distribution.

Using the Gumbel parameters (μ and σ) identified for each loading direction (ψ,θ), the median fatigue strength is computed from Eq. (17) and used to construct the median spherical plot (see Fig. 7d). For the specific case of fully reverse uniaxial tension, regions of lower median fatigue strength are observed at $\theta = 0°$ (parallel to the building direction), while higher median fatigue strengths lie along the equator ($\theta = 90°$, perpendicular to the building direction). The anisotropy is directly linked to the morphology of LoF defects and the relative orientation of the building direction with respect to the macroscopic applied stress Σ_{zz} first principal stress direction. From this median spherical plot, an anisotropic factor, λ is calculated as the ratio between maximum and minimum fatigue strength (equal to 1 for a perfect sphere). In this case, it is equal to 2.49.

$$\text{Median} = \mu - \sigma \ln(\ln(2)) \tag{17}$$

The spherical plot of the μ parameter, which represents the location parameter, identified for the fatigue strengths distribution of LoF defects is plotted as functions of loading directions as illustrated in Fig. 9a. In 9a, high values of μ indicate a high median fatigue strength in these directions (i.e., high-fatigue-strength directions). In contrast, low μ values indicate loading directions with low median fatigue strengths.

Likewise, the spherical plot of the σ parameter, which represents the scale parameter of the fatigue strength distribution (Gumbel model) identified for Lof defects, is plotted as a function of loading directions, as shown in 9b. This parameter quantifies the scale of extreme values or, in other words, the variability and dispersion of the underlying data. From this spherical plot, regions with high σ (yellow regions) indicate greater scatter, while lower σ (blue regions) suggest more concentrated, less dispersed values. When comparing this spherical plot to the median spherical plot of the fatigue strength (refer to Fig. 7d), the loading directions corresponding to higher fatigue strengths exhibit higher variability, whereas the loading directions corresponding to lower fatigue strengths show lower variability. This variability is due to the stress localization differences:

- For loading directions *parallel* to the building direction, corresponding to the lowest fatigue strength, high-stress zones concentrate near the defect equator for all defects, where high curvature promotes severe stress concentration.

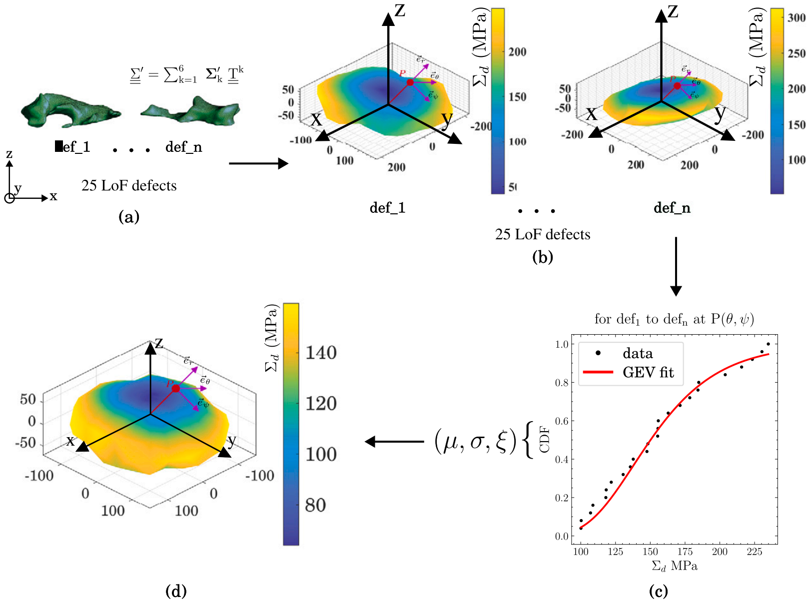

Fig. 7. (a) 25 LoF defect geometries analyzed, (b) fatigue strength spherical plot for each 25 defects, (c) GEV parameter fitting for a given loading direction P(ψ,θ) and (d) illustration of the median HCF strength in the presence of LoF defect population as a function of the loading direction.

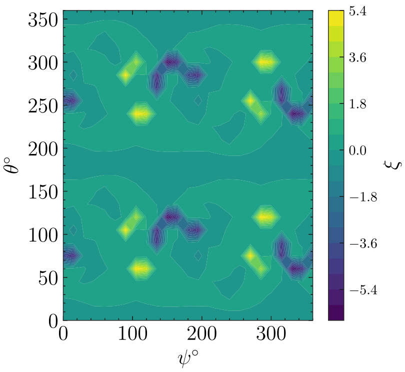

Fig. 8. LoF defects' contour plot of ξ for the loading directions (ψ,θ).

- For loading directions *perpendicular* to the building direction, corresponding to the highest fatigue strengths, high-stress regions differ from one defect to another, increasing scatter.

This is illustrated in Fig. 11, the FIP distribution on the surface of a given LoF defect is subjected to vertical ($\theta = 0°$) and horizontal ($\theta = 90°$) tensile loading (see Fig. 10).

4.1.3. *Analysis of the fatigue strength percentiles*

To visualize the distribution in Euler angles corresponding to low and high-fatigue strength, a *weighted Kernel Density Estimation (KDE)* method is used on angular coordinates (ψ,θ) to determine an estimator of the probability density function involving weights associated to each pair of angles (ψ,θ).

This approach allows to highlight clusters of orientations where low or high fatigue strengths are concentrated, by considering the directions associated to fatigue strength lower than the 10th percentile (P_{10}) of the fatigue strength values, and directions associated to fatigue strength higher than the 90th percentile (P_{90}) of the fatigue strength values, respectively.

The resulting density maps (Fig. 12) show that low-fatigue strength directions (P_{10}) cluster at $\theta = 180°$ or 0°, accounting for symmetry (parallel to the building direction) and high-fatigue strength (P_{90}) are at $\theta = 90°$ or 270°, accounting for symmetry (perpendicular to the building direction). In addition it shows that fatigue strength is more sensitive to the polar angle θ than to the azimuthal angle ψ. Therefore, the statistical analysis presented hereafter will focus on the polar angle θ.

4.1.4. *Non-local analysis*

As detailed in Section 2.3, the macroscopic fatigue strength can be assessed using either a local or a non-local analysis that accounts for the stress gradients, which vary from one defect to another.

A comparison between these two types of approaches is provided in Fig. 13 to assess the impact of the analysis type on the assessed fatigue strength anisotropy. Specifically, it represents the median surface response of the 25 LoF defects corresponding to (a) local analysis and (b) non-local analysis. Moving from local to non-local analysis leads to a reduction in anisotropic factor λ, from 2.49 to 1.53. The anisotropic factor reduction is due to volumetric stress homogenization, which smoothens local stress concentrations due to the tortuous local geometry, thereby decreasing λ compared to the local analysis. Similarly, the normalized variability parameter σ/μ, derived from Gumbel distribution parameters, is significantly reduced in the non-local analysis, illustrated in Fig. 14 as compared to local analysis (see Fig. 10), with σ/μ ranging from 0.18–0.29 for non-local analysis, and 0.19 to 0.41 for local analysis.

Directions with the low fatigue strength ($\leq P_{10}$), noted L_d in the following, cluster at $\theta = 0°$ - parallel to the building direction, and directions with high-fatigue strength ($\geq P_{90}$), noted H_d in the following, cluster at $\theta = 90°$ - perpendicular to the building direction. This confirms that anisotropy directions are intrinsic to defect morphology, even if the non-local analysis reduces the severity of anisotropy. From the percentile analysis (not illustrated in the present paper), directions with low and high fatigue strengths remain consistent between local and non-local analysis. In addition, defect size sensitivity was evaluated for L_d ($\theta = 0°$, $\psi = 90°$) and H_d ($\theta = 90°$, $\psi = 30°$). The evolution of the fatigue strengths with the defect size for these directions is illustrated in Fig. 15 in a Kitagawa–Takahashi diagram. In this figure, defect size ($\sqrt{\text{area}}$) represents the square root of the LoF defect's area projected onto the tensile loading direction. The slopes remain similar across directions.Data for H_d exhibit slightly higher dispersion than L_d, indicating increased variability in localized stress regions from defect morphologies under H_d loading. Numerical results align well

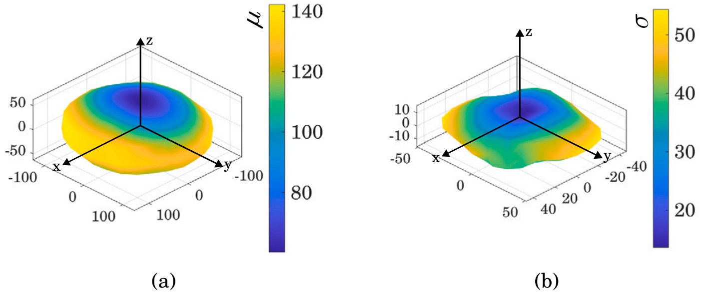

Fig. 9. Spherical plots of the (a) μ and (b) σ parameters for LoF defects loaded in tension.

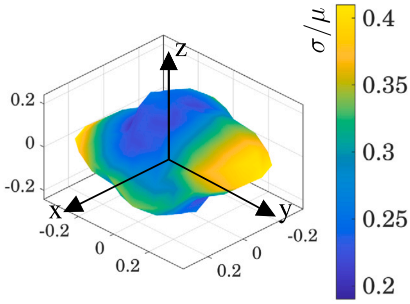

Fig. 10. Relative variability parameter in the presence of LoF defect population as a function of the loading direction — loaded in pure tension.

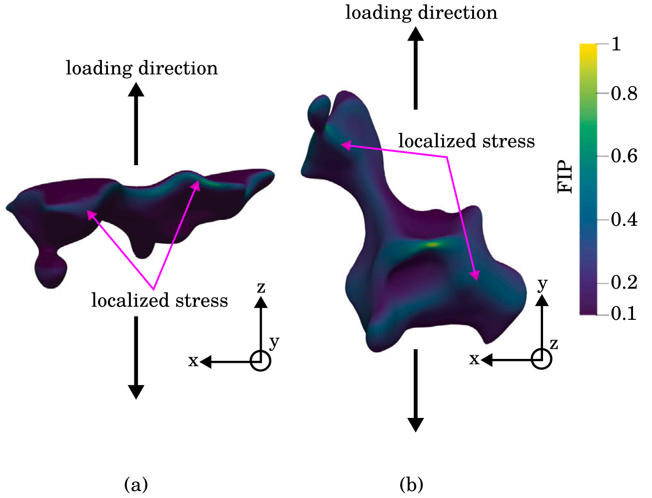

Fig. 11. Localization of areas with high stress concentration for (a) vertical tensile loading and (b) horizontal tensile loading.

with experimental data reported by Bonneric et al. [36], particularly for L_d values. For instance, in both the numerical investigation and Bonneric's experimental study, vertical building direction ($\theta = 0°$) showed the lowest fatigue strengths.

4.2. Gas pores population under tensile loading

A similar analysis was carried out for the 10 considered gas pores. The median value of the HCF strength on gas pores are provided for all the possible loading directions, both local and non-local analyses in Fig. 16a, b. From the local analysis the anisotropic factor $\lambda = 1.27$, it is significantly lower than that of LoF defects (2.49), due to the near-spherical geometry of gas pores. Non-local analysis reduces λ to 1.11, a smaller reduction as compared to LoF defects (from 2.49 to 1.53) which present higher local stress gradients.

Density plots derived from percentile analysis show clustering patterns analogous to LoF defects, and have therefore not been included in the present paper. Low-fatigue strength directions (P_{10}) are at $\theta = 0°$ or 180° (parallel to the building direction), while directions with high-fatigue strength (P_{90}) cluster at $\theta = 90°$ (perpendicular to the building direction). Nevertheless, despite high sphericity gas pores show same anisotropy as LoF defects, in terms of low and high-fatigue strength direction clusters.

The surface plot of normalized variability parameter σ/μ, derived from the Gumbel distribution parameters, is provided in Fig. 16c, d. For the local analysis, the σ/μ values range from 0.06–0.19, indicating lower relative variability compared to LoF defects. The results confirm that numerical analysis captures the reduced morphological variability of gas pores — even with fewer defects sampled (10) than required for LoF defects (25). Transitioning to non-local analysis further reduces the σ/μ range to 0.03–0.14.

4.3. Multiaxial loadings

4.3.1. Influence of third rotation ϕ

As opposed to the pure tension case, the rotated macroscopic stress tensor is impacted by the third rotational angle ϕ when shear and combined tension–shear loadings are considered. As a consequence the fatigue strengths determined for these loading types are sensitive to ϕ angle, as illustrated in Fig. 17. The figure shows the evolution of the fatigue strength of a LoF defect when the ϕ angle evolves from 0° to 360° while the ψ and θ angles are fixed ($\psi = 0°$; $\theta = 0°$), for the cases of shear and combined tension–shear loadings. For this reason the representation of the results as previously proposed for the uniaxial case is not possible since another dimension (ϕ) plays a role on the fatigue strength anisotropy resulting from a defect population.

4.3.2. Interpretation of spherical plot

Following the previous remarks, the problem dimensionality needs to be reduced in order to propose some visualization of the results. As shown in Fig. 17, as the numerical fatigue strength evolves as a function of the angle ϕ, it is proposed to plot the minimum fatigue strength so that the represented fatigue strength is given by: $\Sigma_d(\theta, \psi) = \min_\phi \Sigma_d(\theta, \psi, \phi)$. Similarly to what was done in the case of fully reverse tension, the direction $\mathbf{d}(\theta, \phi)$ represented in the spherical plot is associated with the tensile direction in the case of combined tension/shear. In the case of pure torsion the same representation is chosen and the $\mathbf{d}(\theta, \phi)$ represent the normal to the shear plane.

To further justify this dimensionality reduction, Fig. 18 presents the density distributions of angles θ, ψ, and ϕ for the lowest 10% ($\Sigma_d < P_{10}$) and highest 10% ($\Sigma_d > P_{90}$) fatigue strength values. It can be observed that the ϕ angle exhibits a relatively uniform density distribution compared to θ and ψ, which show stronger variations. This supports the approach of considering only the minimum value across

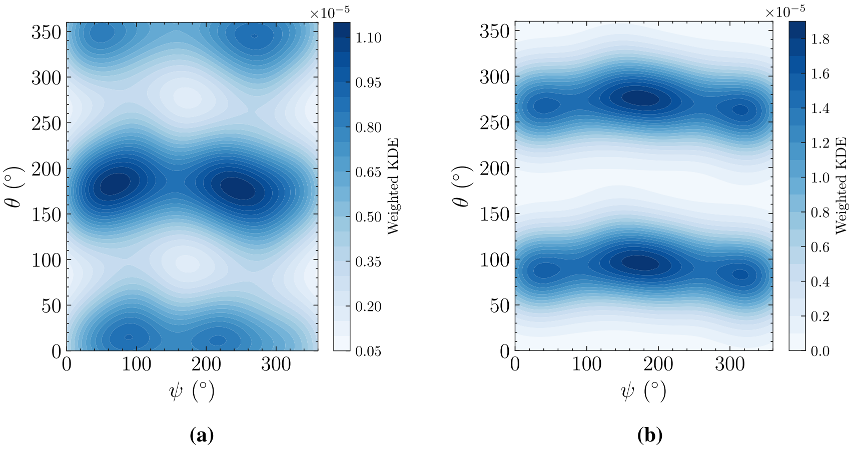

Fig. 12. LoF defects loaded in tension under local analysis — distribution of polar and azimuthal angles corresponding to (a) 10 percentile (P_{10}) fatigue strength values and (b) 90 percentile (P_{90}) fatigue strength values.

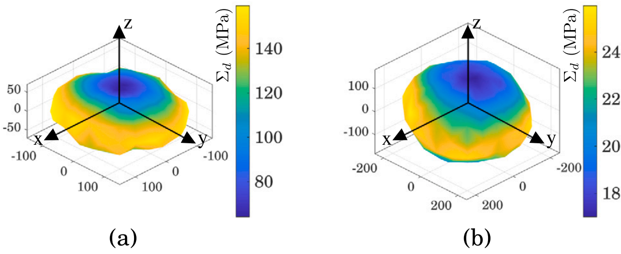

Fig. 13. LoF defects loaded in pure tension–median spherical plots of the fatigue strength in the presence of LoF defects population as a function of the loading direction. (a) local analysis and (b) non-local analysis.

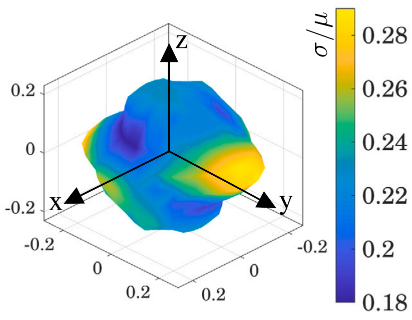

Fig. 14. For a non-local analysis, relative variability parameter in the presence of LoF defect population loaded in pure tension as a function of the loading direction.

ϕ, allowing the spherical representation of the fatigue strengths as a function of θ and ψ only.

Fig. 19 illustrates the mechanical interpretation of how varying the angle ϕ affects the loading direction for a fixed defect orientation. In this schematic, two different ϕ angles at fixed $\psi = 0°$ and $\theta = 45°$ are shown for a gas pore defect. The red arrows represent the rotated macroscopic stress tensor $\underline{\underline{\Sigma}}'$, and highlight how the orientation of the shear components (dotted blue) evolve around the fixed defect. This confirm the need for evaluating the worst-case fatigue strength (minimum) by considering all the possible ϕ rotations for each (θ, ψ) direction.

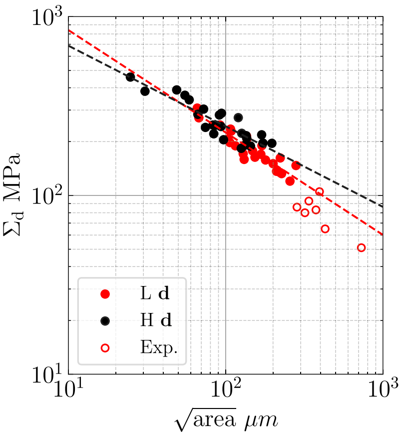

Fig. 15. Non-local analysis of LoF defects loaded under tension — Variation of fatigue strengths with defect size in a log–log scale, at both lowest and highest-fatigue strength directions.

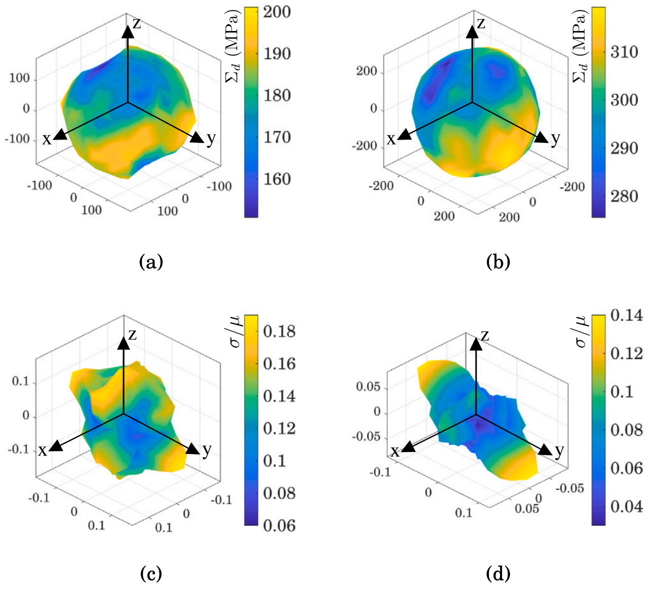

Fig. 16. Median spherical plots of fatigue strength (a, b) and relative variability parameter (c, d) for gas pores under pure tension loading, evaluated using (a, c) local analysis ($\lambda = 1.27$) and (b, d) non-local analysis ($\lambda = 1.11$).

Table 1
Fatigue strengths of vertical ($\theta = 0°$) and horizontal ($\theta = 90°$), and their resulting anisotropic factors λ for high and low ductility materials reported in the literature.

Material	$\theta = 0°$ Σ_{max}	$\theta = 90°$ Σ_{max}	Load ratio R	λ	Ductility	Failure from	References
L-PBF AlSi10Mg	50	127	0.1	2.54	High	LoF defects	[29]
	108	160	0.1	1.48		LoF defects	[48]
	112	153	0	1.37		LoF defects	[49]
	193	244	0.1	1.26		Gas pores	[50]
L-PBF SS 316L	147	388	0.1	2.64		LoF defects	[51]
L-PBF 17-4PH	200	260	−1	1.30	Low	LoF defects	[52]
DMLS maraging steel MS1	219	240	−1	1.10		Gas pores	[53]
L-PBF 15-5 PH SS	248	300	−1	1.21		LoF defects	[54]
L-PBF Ti–6Al–4V	100	200	−0.2	2.00		Gas pores	[55]
	346	439	−1	1.27		Gas pores	[56]
	–	–	0.1	1.63		Gas pores	[57]

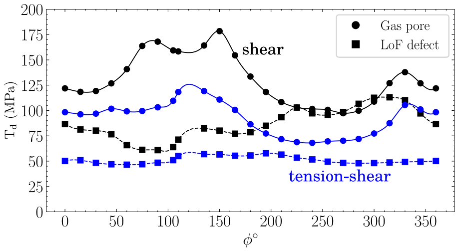

Fig. 17. Variation in fatigue strength as a function of ϕ at a fixed ($\psi = 0°$ and $\theta = 0°$) for both gas pore and LoF defects under shear and combined proportional tension–shear loading.

4.3.3. Fatigue strength anisotropy in presence of defects for fully reverse shear loading

Median LoF defects' spherical plots (Fig. 20a, b) confirm weaker anisotropy, with λ decreasing from 1.28 (local) to 1.09 (non-local) - a 15% reduction. This contrasts sharply with fully reverse tension, where λ decreased by 39% (2.49 to 1.53). This also shows that shear loading results in less anisotropy than tension loading. From the gas pores' median spherical plots (Fig. 20c, d), λ decreasing from 1.29 (local) to 1.1 (non-local), a 15% reduction, similarly to LoF defects.

The normalized variability parameter σ/μ for LoF defects under shear loading exhibits a range of 0.2–0.3 in local analysis, narrowing to 0.19–0.25 in non-local analysis (Fig. 21a, b). Gas pores exhibit even lower variability, with σ/μ ranging 0.06–0.16 (local) and 0.02–0.12 (non-local) (Fig. 21c, d).

In order to better identify the regions of high/low fatigue strength a percentile analysis is proposed. It considers all fatigue strengths, including the full distribution of fatigue strengths for every (θ, ψ, ϕ) combination. This approach preserves impact of all the rotation angles, allowing precise identification of low and high-fatigue strength directions clusters across all orientations. Fig. 22a presents the density map of the angles ψ and θ that are associated to fatigue strengths whose values at or below the 10th percentile (i.e., ($\leq P_{10}$)). The cluster peaks observed in this map therefore correspond to the directions associated with low fatigue strength. Notably, these peaks align with specific combinations of polar and azimuthal angles ($\theta = +/-45°, \psi = +/-90°$), which correspond to the directions of the maximum principal stresses acting under shear conditions. A similar analysis conducted on the upper 90th percentile values (i.e., $\geq P_{90}$) reveals cluster peaks at $\theta = 90°$ and $\psi = 0°$ (Fig. 22b), indicating that this orientation is associated with the highest fatigue strength under the same loading conditions. Furthermore, the non-local analysis do not modifies Ld and Hd that are consistent with local the ones identified from the local analyses.

For gas pores, the analysis of low-fatigue-strength directions (P_{10}) under shear loading (not illustrated in this paper) shows peak orientations similar to those identified for LoF defects, in both local and non-local analysis. However, differences arise when examining the directions associated with high fatigue strength (P_{90}). In the local analysis, the cluster peak is located at $\theta = 120°$ and $\psi = 135°$, whereas in the non-local analysis, the peak shifts to $\theta = 90°$ and $\psi = 0°$ - which is consistent with LoF defects' high-fatigue strength directions.

4.3.4. Fatigue strength anisotropy in presence of defects for proportional combined tension–shear loading

Median LoF defects' spherical plots (Fig. 23a, b) shows anisotropy for LoF defects, with λ decreasing from 1.57 (local) to 1.15 (non-local) - a 27% reduction. Gas pores show a similar trend, with lower initial anisotropy: λ decreases from 1.23 (local) to 1.08 (non-local), a 12% reduction (Fig. 23c, d).

The normalized variability parameter σ/μ for LoF defects under combined tension–shear loading ranges between 0.18–0.31 in local analysis, narrowing to 0.19–0.25 in non-local analysis (Fig. 24a, b). Gas pores exhibit significantly lower relative variability, with σ/μ values ranging 0.06–0.16 (local) and 0.03–0.12 (non-local) (Fig. 24c, d).

Similar to the pure shear case, the percentile analysis considers all fatigue strengths across ϕ orientations: $\Sigma_d(\theta, \psi, \phi)$, retaining the full distribution of fatigue strengths for every (θ, ψ, ϕ) combination. For LoF defects in the local analysis, the cluster peaks of orientations corresponding to the lowest fatigue strengths ($\leq P_{10}$) values occurs at specific combinations of polar and azimuthal angles (θ, ψ), which correspond to the directions of the maximum principal stresses acting under combined tension–shear ($T_a/\Sigma_a = 1$) loading conditions (Fig. 25a). The cluster peaks of orientations corresponding to the highest fatigue strengths ($\geq P_{90}$) are $\theta = 90°$ and $\psi = 0°$, corresponding to high-fatigue strength directions (Fig. 25b). Non-local analysis retains these directional trends, indicating that volumetric stress homogenization does not change the principal directions corresponding to low and high-fatigue strengths.

Gas pores, however, exhibit distinct behavior in the local analysis: the highest fatigue strengths correspond to $\theta = 60°$ and $\psi = 60°$, diverging from the trends observed for LoF defects. Nevertheless, non-local analysis shifts this high-strength directions to $\theta = 90°$ and $\psi = 0°$, bringing it into alignment with the high-strength directions of LoF defects. This suggests that volumetric stress homogenization reduces defect-induced HCF strength anisotropy, smoothing out local geometric effects under combined tension–shear loading, similar to what was observed in the pure shear loading case. Meanwhile, the directions with low-fatigue strength for gas pores remain consistent with the principal stress directions, similar to LoF defects.

5. Discussion summary

This section focuses on summarizing the results obtained under three different loading conditions, comparing both defect types.

The reported anisotropic factor λ in literature differs between materials categorized as high-ductility and low-ductility. In this work, materials exhibiting an elongation (A%) greater than 20% are classified

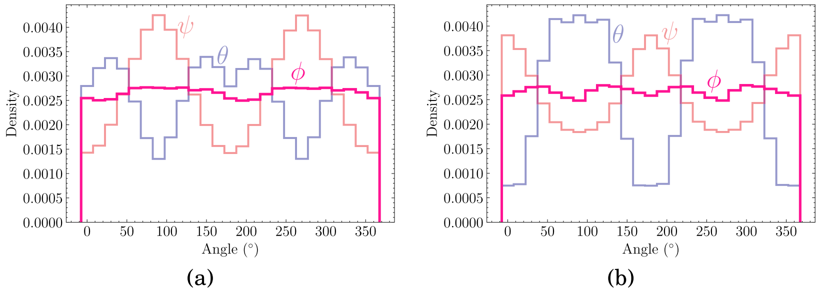

Fig. 18. Density distributions of angles θ, ψ, and ϕ among directions corresponding to (a) the lowest 10% and (b) the highest 10% fatigue strength values — LoF defects loaded in pure shear.

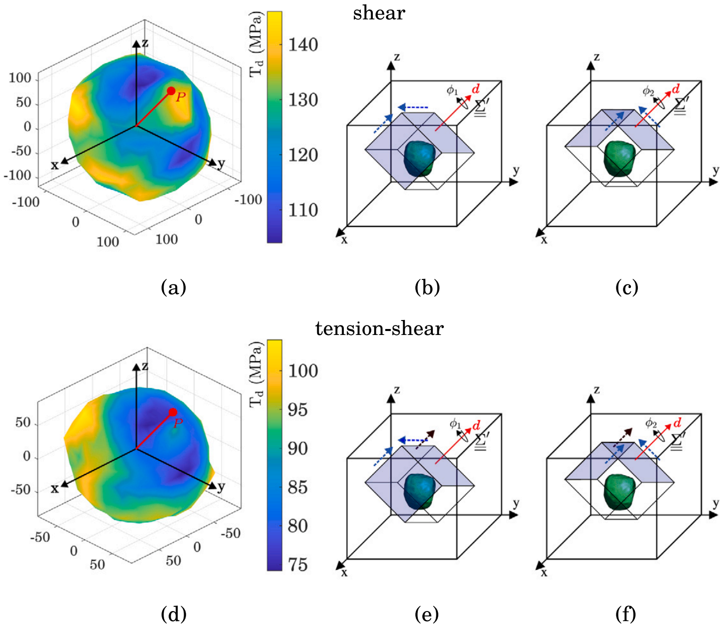

Fig. 19. (a, b, c) Shear and (d, e, f) Combined tension–shear loading type's spherical plot of a gas pore. At point P, illustration of loading direction $\underline{\underline{\Sigma}}'$ in red, with respect to gas pore whose orientation is fixed for two different $\phi(= 0$ and $-90)$ angles at a specific ψ and θ angles, which are 0 and 45° respectively. Shear loading directions are in dotted blue lines and tensile loading directions are in dotted black lines.

as high-ductility, whereas those with A% below 20% are considered low-ductility. High-ductility materials exhibit a broader anisotropic factor range (1.26–2.64) compared to low-ductility materials (1.10–2.00), as summarized in Table 1. This difference could be attributed to the limited ability of low-ductility materials to undergo plastic deformation and redistribute stresses around defects. LoF defects become more critical under positive load ratios ($R \geq 0$), where tensile loading increases defect sensitivity, leading to pronounced anisotropy in fatigue strength. For instance, studies on AlSi10Mg [29] and SS 316L [51], both highly ductile, report high λ values of up to 2.54 and 2.64, respectively, and indicate LoF defects as the dominant failure origin. It should be noted that the reported range of anisotropic factors (λ) depends on material properties such as ductility and defect type; while the absolute values differ between materials, the qualitative trend of increased anisotropy associated with LoF defects under tensile loading is generally observed.

The numerical results are in agreement with the literature. For LoF defects, both local ($\lambda = 2.49$) and non-local ($\lambda = 1.53$) anisotropy factors fall within the established literature range of 1.21–2.64. Similarly, for gas pores, both local ($\lambda = 1.27$) and non-local ($\lambda = 1.11$) values are within the reported experimental range of 1.10–2.00.

Table 2 shows the summary of the impact of loading directions under tension, shear, and combined tension–shear loading cases for two defect types from the non-local analysis. For each loading type, it has been categorized into lowest and highest-fatigue strength loading directions, which were identified from the non-local analysis KDE analysis or percentile analysis discussed in the previous section, when considering non-local fatigue criterion (4).

To evaluate the statistical distribution of fatigue strengths in critical and non-critical loading directions for both defect types, empirical cumulative distribution functions (ECDFs) were plotted, as shown in Fig. 26. The fatigue strengths at lowest and highest-fatigue strength were extracted for each defect geometry at a fixed ψ, θ, and this process was repeated for all the considered defect geometries. Using these extracted fatigue strength values, CDFs were generated to analyze the statistical distributions.

Regardless of the loading or defect type, the highest-fatigue strength direction (i.e., the orientation of the direction vector **d**) corresponds to $\theta = 90°$. However, the difference in fatigue strengths at the median value (ECDF = 0.5) between the lowest and highest-fatigue strength directions is more pronounced in tension than in other loading types. When defect morphology is considered, the difference in median fatigue strengths between LoF defects and gas pores is also greater in tension for both anisotropy directions. These observations suggest that the tension case is more sensitive to changes in both loading direction and defect morphology. For LoF defects, comparing the tension case with shear and combined tension–shear cases shows a shift in the critical loading directions from $\theta = 0°$ to $\theta = 45°$, $\psi = 90°$ and $\theta = 30°$, $\psi = 90°$ respectively.

Table 2

Lowest (L) and highest (H) fatigue strength directions (polar θ and azimuthal ψ angles) under different loading conditions for both defect types from the non-local analysis.

Defect type	Tension		Shear		Tension–Shear	
	L	H	L	H	L	H
LoF defects/Gas pores	$\theta = 0°$	$\theta = 90°$	$\theta = 45°,\ \psi = 90°$	$\theta = 90°,\ \psi = 0°$	$\theta = 30°,\ \psi = 90°$	$\theta = 90°,\ \psi = 0°$

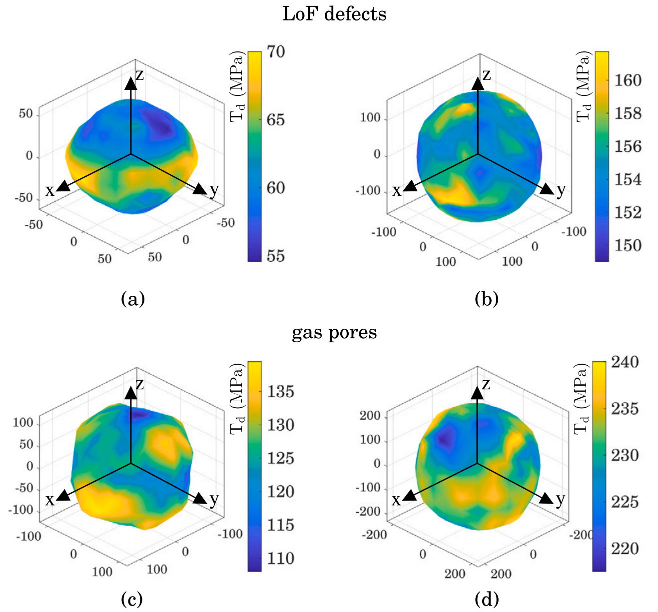

Fig. 20. Median spherical plots of fatigue strength under pure shear loading for LoF defects and gas pores. (a) Local analysis of LoF defects ($\lambda = 1.28$), (b) Non-local analysis of LoF defects ($\lambda = 1.09$), (c) Local analysis of gas pores ($\lambda = 1.29$), and (d) Non-local analysis of gas pores ($\lambda = 1.10$).

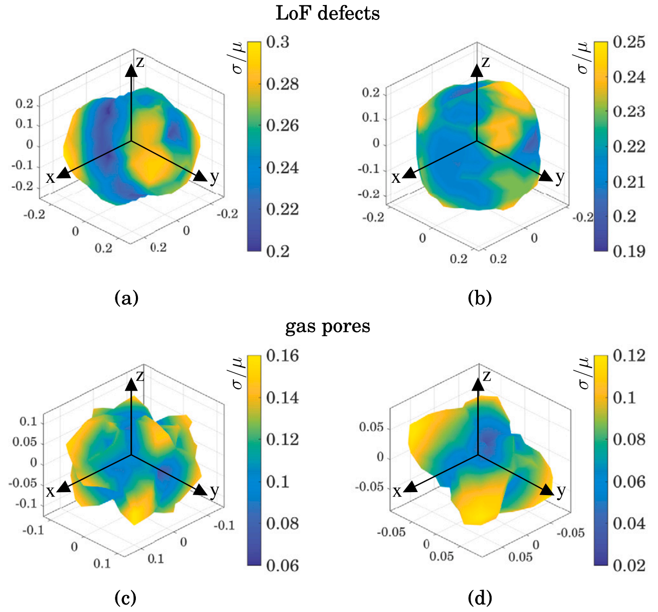

Fig. 21. Relative variability parameter σ/μ as a function of loading direction under pure shear loading for (a, b) LoF defects and (c, d) gas pores, evaluated using (a, c) local and (b, d) non-local analysis.

The comparison of the anisotropic factor (λ) under different loading types for both LoF defects and gas pores, based on local and non-local analysis, is shown in Fig. 27a. From this figure, it can be observed that for LoF defects, λ is higher in tension compared to shear and proportional combined tension–shear loading conditions, in both local and non-local analyses. However, for gas pores which are more spherical in nature, there is no major difference in λ among the three considered loading conditions, regardless of whether local or non-local analysis is applied. When comparing λ between LoF defects and gas pores across all loading conditions, the difference is most pronounced in tension, followed by combined tension–shear, while the shear case shows no change even with their surface responses being different. These observations suggest, as also noted earlier from the density plot analyses, that changes in loading direction and morphology have a higher impact under tension compared to the other loading types.

The percentage change or decrease of λ (denoted as $\%\Delta\lambda$) from local (L) to non-local (NL) analyses is illustrated in Fig. 27b for both defect types under tension, shear, and tension–shear loading conditions. The non-local analysis allows the smoothing of the surface response by averaging the stresses on and around the defect geometry over a given volume, V_c. For LoF defects, when subjected to tension which exhibits a high anisotropic surface response in the local analysis, the $\%\Delta\lambda$ from local to non-local analysis is the highest compared to other loading conditions. This is likely due to the higher stress concentration factors in tension, as compared to shear [58] and proportional combined tension–shear, and the resulting steep stress gradients (which vary with defect sizes). Consequently, even with a small non-local parameter d_c (6 μm), the stresses surrounding the defects are significantly reduced. On the contrary, for gas pores, which exhibit a highly isotropic morphology, the $\%\Delta\lambda$ from local to non-local analyses is similar across all loading conditions.

Fig. 28 illustrates the workflow for optimized build-direction part fabrication aimed at increasing fatigue resistance. FE analysis of the component is first used to identify the most highly stressed zone and the corresponding loading condition at that zone. Based on defect statistics in this critical region, representative defects are selected for FE simulations. For each considered defect population, fatigue strengths are computed as a function of orientations. Using extreme value statistics, Gumbel parameters are fitted to the empirical data. This allows the construction of low fatigue strength regions density maps, which in turn guide the optimization of the part's build direction for the specified loading condition.

6. Conclusions and perspectives

Based on the results of the numerical investigation, the following conclusions can be drawn:

- Fatigue strength is more sensitive to the polar angle θ than to the azimuthal angle ψ, especially in pure tension case. The fatigue strength anisotropy is likely due to the morphology of defect geometries ranging from low sphericity (LoF defects) to high sphericity (gas pores) and their fixed orientation relative to the loading direction or direction vector **d**.
- The morphology factor is less dominant in shear loading than in tensile loading. Tensile loading is more sensitive to changes in both the loading direction and defect morphology.

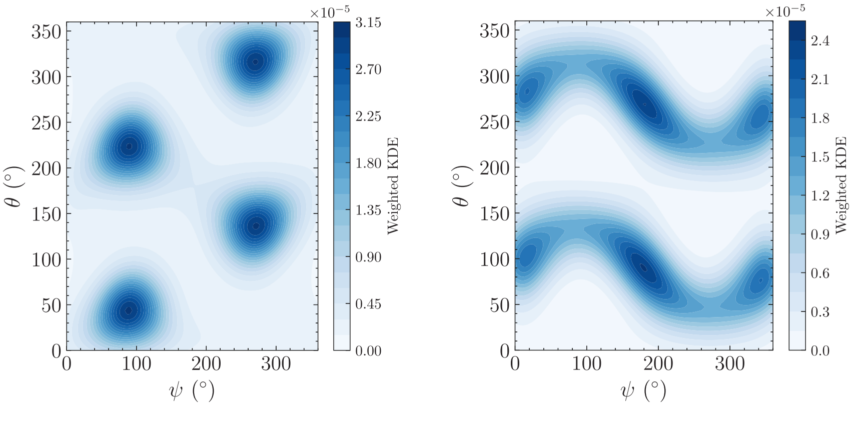

(a) (b)

Fig. 22. For a local analysis at LoF defects loaded under fully reversed shear — Distribution of (a) the 10 percentile (P_{10}) fatigue strength values and (b) the 90 percentiles (P_{90}) fatigue strength values for LoF defects depending on the polar (θ) and azimuthal (ψ) angles.

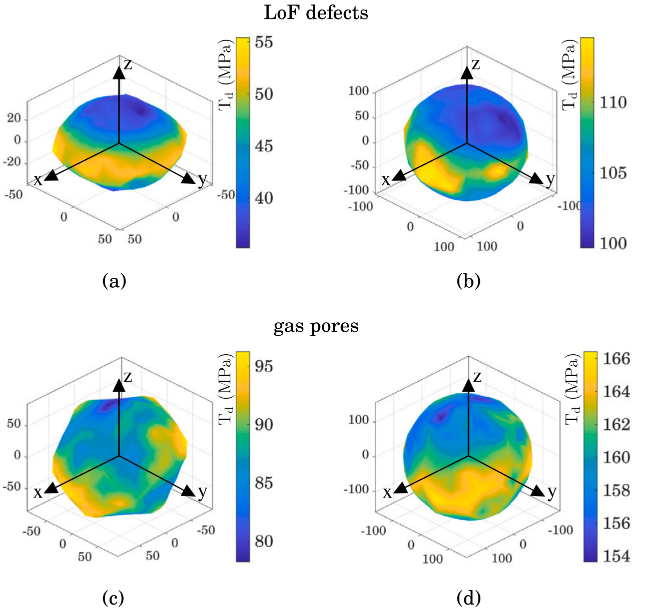

Fig. 23. Median spherical plots of the fatigue strength under proportional combined tension–shear loading ($T_a/\Sigma_a = 1$) for (a, b) LoF defects and (c, d) gas pores, evaluated using (a, c) local analysis with $\lambda = 1.57$ and 1.23, respectively, and (b, d) non-local analysis with $\lambda = 1.15$ and 1.08, respectively.

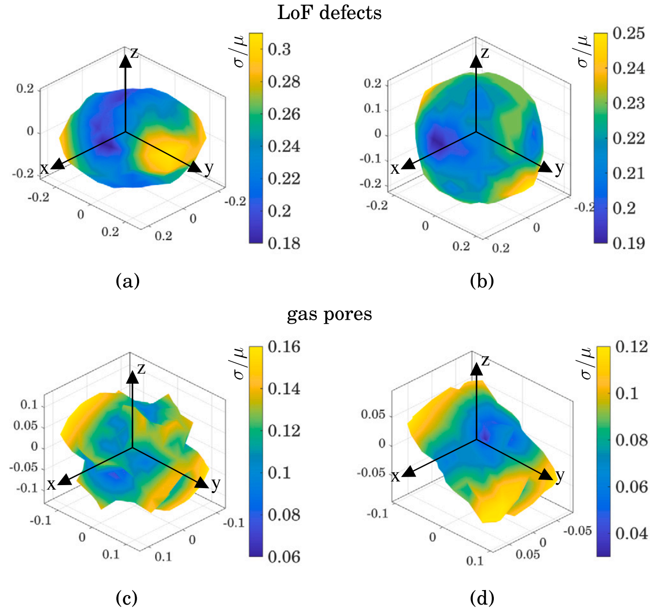

Fig. 24. Relative variability parameter (σ/μ) as a function of the loading direction under proportional combined tension–shear loading ($T_a/\Sigma_a = 1$) for (a, b) LoF defects and (c, d) gas pores, evaluated using (a, c) local and (b, d) non-local analysis.

- From the percentile analysis, regardless of the loading type or defect morphology, the non-critical loading direction is consistently observed at $\theta = 90°$ (aligned with the *xy*-plane).
- A non-local analysis was conducted to account for stress gradients around the defect geometries by averaging stresses over a given volume V_c, the surface response was smoothened, leading to a reduction in the anisotropy factor.
- The relative variability parameter σ/μ showed that stress variability is strongly influenced by defect morphology and loading type. For LoF defects, tension loading was associated with the highest initial σ/μ range (0.19–0.41), indicating significant stress localization. Non-local analysis reduced this range by 29% (to 0.18–0.29). Shear and combined tension–shear loadings showed smaller reductions (17%–19%). Gas pores exhibited much lower initial σ/μ values (0.06–0.19 in tension) and consistent reductions of approximately 26% under non-local analysis across all loading modes.

This study assumes a linear elastic isotropic material and applies a multiaxial HCF strength criterion (Crossland) that is known to give good results only for proportional loadings. Future work should extend the current study by incorporating elastic–plastic behavior and validating fatigue prediction models applicable to both proportional and non-proportional multiaxial loadings.

Additionally, the current study does not account for the influence of the loading ratio, which plays a role in determining the proportion of fatigue life governed by short crack propagation. This, in turn, impacts both fatigue strength and fatigue life. Future studies should address

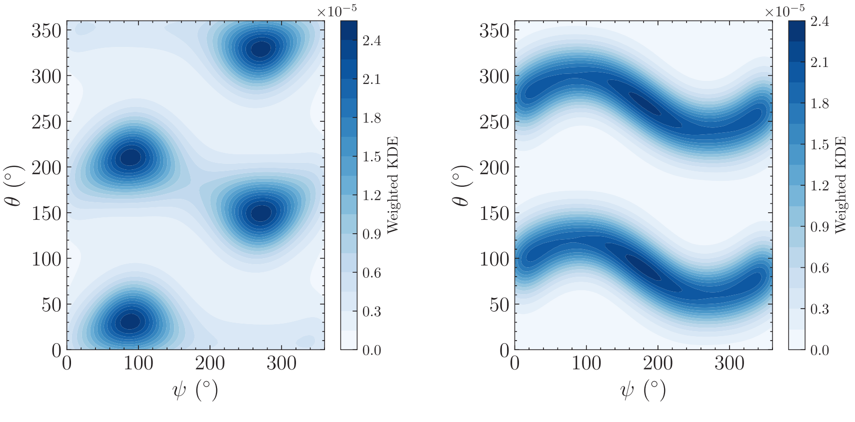

(a)

(b)

Fig. 25. For a local analysis at LoF defects loaded under fully reversed combined tension–shear ($T_a/\Sigma_a = 1$) - Distribution of (a) the 10 percentile (P_{10}) fatigue strength values and (b) the 90 percentiles (P_{90}) fatigue strength values for LoF defects depending on the polar (θ) and azimuthal (ψ) angles.

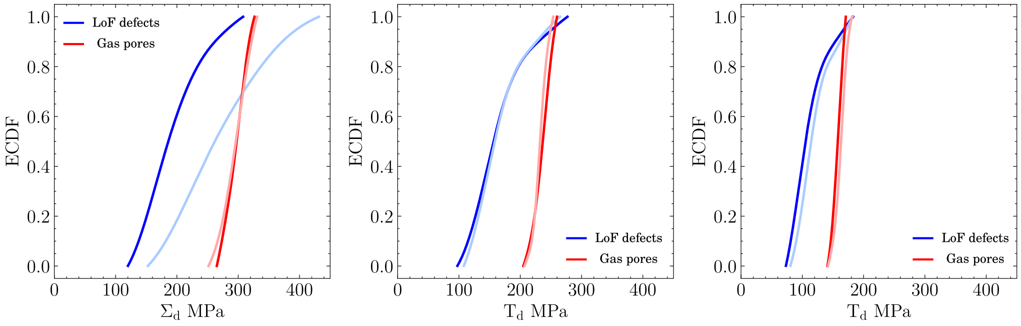

(a)

(b)

(c)

Fig. 26. From non-local analysis, CDFs of low-fatigue strength direction (in blue and red) and high-fatigue strength direction (in transparent blue and red) loading directions in both LoF defects and gas pores loaded under (a) tension, (b) shear and (c) proportional combined tension–shear ($T_a/\Sigma_a = 1$).

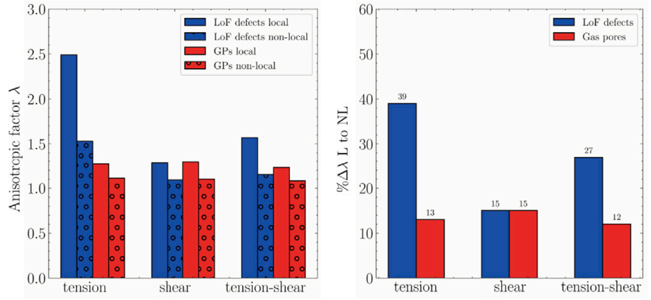

(a)

(b)

Fig. 27. Under different loading types for both populations of defects (a) comparison of anisotropic factor (λ) in local and non-local analysis and (b) % decrease of λ from local (L) to non-local (NL) analysis.

this aspects by considering the effect of loading ratio on short crack propagation and its interaction with anisotropic HCF strength across different building orientations.

Capturing position/depth-dependent effects of LoF defects represents an important research prospect particularly for materials where the short crack propagation may play an important role in the overall fatigue life.

CRediT authorship contribution statement

Sai Sreenivas Penkulinti: Writing – original draft, Validation, Methodology, Investigation. **Nicolas Saintier:** Writing – review & editing, Validation, Supervision, Project administration, Methodology, Funding acquisition, Conceptualization. **Matthieu Bonneric:** Writing – review & editing, Supervision, Project administration, Methodology, Conceptualization. **Benoit Verquin:** Writing – review & editing, Validation, Project administration. **Thierry Palin-Luc:** Writing – review & editing, Validation. **Fabien Lefebvre:** Writing – review & editing. **Pascal Ghys:** Writing – review & editing.

Declaration of competing interest

The authors declare that they have no known competing financial interests or personal relationships that could have appeared to influence the work reported in this paper.

Acknowledgments

The authors acknowledge the financial support of CETIM, France, for this study. The experimental work was performed on the Durability Platform of the I2M Institute. Fatigue samples were produced on the FUTURPROD, additive manufacturing platform at the I2M institute.

Data availability

The data that has been used is confidential.

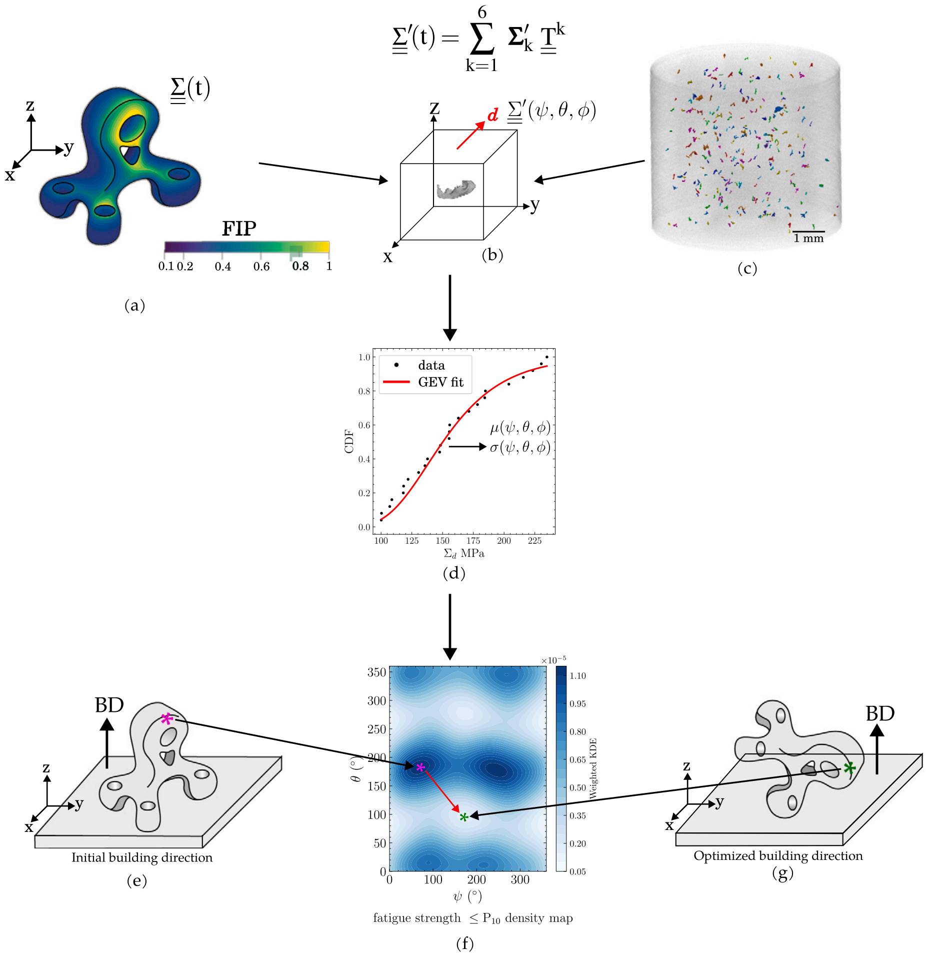

Fig. 28. A workflow for optimized-building direction part fabrication (a) FEA of the part, (b) FE calculations, (c) knowledge of defect statistics, (d) extreme value statistics, (e) initial building direction, (f) low fatigue strength directions density map and (g) optimized building direction.

References

[1] Mostafaei A, Zhao C, He Y, Reza Ghiaasiaan S, Shi B, Shao S, Shamsaei N, Wu Z, Kouraytem N, Sun T, Pauza J, Gordon JV, Webler B, Parab ND, Asherloo M, Guo Q, Chen L, Rollett AD. Defects and anomalies in powder bed fusion metal additive manufacturing. Curr Opin Solid State Mater Sci 2022;26(2):100974. http://dx.doi.org/10.1016/j.cossms.2021.100974, URL https://www.sciencedirect.com/science/article/pii/S1359028621000772.

[2] Li E, Wang L, Yu A, Zhou Z. A three-phase model for simulation of heat transfer and melt pool behaviour in laser powder bed fusion process. Powder Technol 2021;381:298–312. http://dx.doi.org/10.1016/j.powtec.2020.11.061, URL https://www.sciencedirect.com/science/article/pii/S0032591020311207.

[3] Tammas-Williams S, Zhao H, Léonard F, Derguti F, Todd I, Prangnell P. Xct analysis of the influence of melt strategies on defect population in Ti–6Al–4V components manufactured by selective electron beam melting. Mater Charact 2015;102:47–61. http://dx.doi.org/10.1016/j.matchar.2015.02.008, URL https://www.sciencedirect.com/science/article/pii/S104458031500039X.

[4] DebRoy T, Wei H, Zuback J, Mukherjee T, Elmer J, Milewski J, Beese A, Wilson-Heid A, De A, Zhang W. Additive manufacturing of metallic components – process, structure and properties. Prog Mater Sci 2018;92:112–224. http://dx.doi.org/10.1016/j.pmatsci.2017.10.001, URL https://www.sciencedirect.com/science/article/pii/S0079642517301172.

[5] Kouraytem N, Li X, Cunningham R, Zhao C, Parab N, Sun T, Rollett AD, Spear AD, Tan W. Effect of laser-matter interaction on molten pool flow and keyhole dynamics. Phys Rev Appl 2019;11:064054. http://dx.doi.org/10.1103/PhysRevApplied.11.064054, URL https://link.aps.org/doi/10.1103/PhysRevApplied.11.064054.

[6] Sames WJ, List FA, Pannala S, Dehoff RR, Babu SS. The metallurgy and processing science of metal additive manufacturing. Int Mater Rev 2016;61(5):315–60. http://dx.doi.org/10.1080/09506608.2015.1116649.

[7] Murakami Y. Metal fatigue: effects of small defects and nonmetallic inclusions. Elsevier; 2002.

[8] Khoukhi DE, Morel F, Saintier N, Bellett D, Osmond P, Le V-D. Probabilistic modeling of the size effect and scatter in high cycle fatigue using a Monte-Carlo approach: Role of the defect population in cast aluminum alloys. Int J Fatigue 2021;147:106177. http://dx.doi.org/10.1016/j.ijfatigue.2021.106177, URL https://www.sciencedirect.com/science/article/pii/S0142112321000372.

[9] Wilson P, Saintier N, Palin-Luc T, Sudret B, Bergamo S. Statistical study of the size and spatial distribution of defects in a cast aluminium alloy for the low fatigue life assessment. Int J Fatigue 2022;166:107206. http://dx.doi.org/10.1016/j.ijfatigue.2022.107206.

[10] Ben Sghaier R, Bouraoui C, Fathallah R, Hassine T, Dogui A. Probabilistic high cycle fatigue behaviour prediction based on global approach criteria. Int J Fatigue 2007;29(2):209–21. http://dx.doi.org/10.1016/j.ijfatigue.2006.03.015, URL https://www.sciencedirect.com/science/article/pii/S014211230600137X.

[11] Koutiri I, Bellett D, Morel F, Augustins L, Adrien J. High cycle fatigue damage mechanisms in cast aluminium subject to complex loads. Int J Fatigue 2013;47:44–57. http://dx.doi.org/10.1016/j.ijfatigue.2012.07.008, URL https://www.sciencedirect.com/science/article/pii/S0142112312002356.

[12] Shiozawa K, Morii Y, Nishino S, Lu L. Subsurface crack initiation and propagation mechanism in high-strength steel in a very high cycle fatigue regime. Int J Fatigue 2006;28(11):1521–32. http://dx.doi.org/10.1016/j.ijfatigue.2005.08.015, Third International Conference on Very High Cycle Fatigue (VHCF-3). URL https://www.sciencedirect.com/science/article/pii/S0142112306000995.

[13] Murakami Y, Endo M. Effects of defects, inclusions and inhomogeneities on fatigue strength. Int J Fatigue 1994;16(3):163–82. http://dx.doi.org/10.1016/0142-1123(94)90001-9, URL https://www.sciencedirect.com/science/article/pii/0142112394900019.

[14] Liu QC, Elambasseril J, Sun SJ, Leary M, Brandt M, Sharp PK. The effect of manufacturing defects on the fatigue behaviour of Ti-6Al-4V specimens fabricated using selective laser melting. In: 11th international fatigue congress. Advanced materials research, vol. 891, Trans Tech Publications Ltd; 2014, p. 1519–24. http://dx.doi.org/10.4028/www.scientific.net/AMR.891-892.1519.

[15] Serrano-Munoz I, Buffiere J-Y, Mokso R, Verdu C, Nadot Y. Location, location & size: Defects close to surfaces dominate fatigue crack

initiation. Sci Rep 2017;7. http://dx.doi.org/10.1038/srep45239, URL https://www.scopus.com/inward/record.uri?eid=2-s2.0-85016314399&doi=10.1038%2fsrep45239&partnerID=40&md5=702d4c22c097ff968c5a29e230ab430e.

[16] El Khoukhi D, Morel F, Saintier N, Bellett D, Osmond P, Le V-D, Adrien J. Experimental investigation of the size effect in high cycle fatigue: Role of the defect population in cast aluminium alloys. Int J Fatigue 2019;129:105222. http://dx.doi.org/10.1016/j.ijfatigue.2019.105222, URL https://www.sciencedirect.com/science/article/pii/S0142112319303263.

[17] Wang QG, Crepeau PN, Davidson CJ, Griffiths JR. Oxide films, pores and the fatigue lives of cast aluminum alloys. Met Mater Trans B 2006;37(6). http://dx.doi.org/10.1007/BF02735010.

[18] Koutiri I, Pessard E, Peyre P, Amlou O, De Terris T. Influence of slm process parameters on the surface finish, porosity rate and fatigue behavior of as-built inconel 625 parts. J Mater Process Technol 2017;255. http://dx.doi.org/10.1016/j.jmatprotec.2017.12.043.

[19] Buffiere J-y, Savelli S, Jouneau P-H, Maire E, Fougeres R. Experimental study of porosity and its relation to fatigue mechanisms of model Al-Si7-MgO.3 cast Al alloys. Mater Sci Eng: A 2001;316:115–26. http://dx.doi.org/10.1016/S0921-5093(01)01225-4.

[20] Yadollahi A, Shamsaei N, Thompson SM, Elwany A, Bian L. Effects of building orientation and heat treatment on fatigue behavior of selective laser melted 17-4 ph stainless steel. Int J Fatigue 2017;94:218–35. http://dx.doi.org/10.1016/j.ijfatigue.2016.03.014, Fatigue and Fracture Behavior of Additive Manufactured Parts. URL https://www.sciencedirect.com/science/article/pii/S0142112316300202.

[21] Mower TM, Long MJ. Mechanical behavior of additive manufactured, powder-bed laser-fused, materials. Materials Science and Engineering: A 2016;651:198–213. http://dx.doi.org/10.1016/j.msea.2015.10.068, URL https://www.sciencedirect.com/science/article/pii/S092150931530530X.

[22] Yamashita Y, Murakami T, Mihara R, Okada M, Murakami Y. Defect analysis and fatigue design basis for Ni-based superalloy 718 manufactured by selective laser melting. Int J Fatigue 2018;117:485–95. http://dx.doi.org/10.1016/j.ijfatigue.2018.08.002, URL https://www.sciencedirect.com/science/article/pii/S0142112318303438.

[23] Borbély A, Mughrabi H, Eisenmeier G, Höppel HW. A finite element modelling study of strain localization in the vicinity of near-surface cavities as a cause of subsurface fatigue crack initiation. Int J Fract 2002;115(3):227–32.

[24] Xu Z, Wen W, Zhai T. Effects of pore position in depth on stress/strain concentration and fatigue crack initiation. Met Mater Trans A 2011;43. http://dx.doi.org/10.1007/s11661-011-0947-x.

[25] Billaudeau T, Nadot Y, Bezine G. Multiaxial fatigue limit for defective materials: mechanisms and experiments. Acta Mater 2004;52(13):3911–20. http://dx.doi.org/10.1016/j.actamat.2004.05.006, URL https://www.sciencedirect.com/science/article/pii/S135964540400268X.

[26] Léopold G, Nadot Y, Billaudeau T, Mendez J. Influence of artificial and casting defects on fatigue strength of moulded components in Ti-6Al-4V alloy. Fatigue Fract Eng Mater Struct 2015;38(9):1026–41. http://dx.doi.org/10.1111/ffe.12326, arXiv:https://onlinelibrary.wiley.com/doi/pdf/10.1111/ffe.12326, URL https://onlinelibrary.wiley.com/doi/abs/10.1111/ffe.12326.

[27] Rotella A, Nadot Y, Piellard M, Augustin R, Fleuriot M. Influence of defect morphology and position on the fatigue limit of cast Al alloy: 3d characterization by x-ray microtomography of natural and artificial defects. Mater Sci Eng: A 2020;785:139347. http://dx.doi.org/10.1016/j.msea.2020.139347, URL https://www.sciencedirect.com/science/article/pii/S0921509320304287.

[28] Sun W, Ma Y, Huang W, Zhang W, Qian X. Effects of build direction on tensile and fatigue performance of selective laser melting Ti6Al4V titanium alloy. Int J Fatigue 2020;130:105260. http://dx.doi.org/10.1016/j.ijfatigue.2019.105260, URL https://www.sciencedirect.com/science/article/pii/S0142112319303640.

[29] Wu Z, Wu S, Bao J, Qian W, Karabal S, Sun W, Withers PJ. The effect of defect population on the anisotropic fatigue resistance of AlSi10Mg alloy fabricated by laser powder bed fusion. Int J Fatigue 2021;151:106317. http://dx.doi.org/10.1016/j.ijfatigue.2021.106317, URL https://www.sciencedirect.com/science/article/pii/S0142112321001778.

[30] Larrosa N, Wang W, Read N, Loretto M, Evans C, Carr J, Tradowsky U, Attallah M, Withers P. Linking microstructure and processing defects to mechanical properties of selectively laser melted AlSi10Mg alloy. Theor Appl Fract Mech 2018;98:123–33. http://dx.doi.org/10.1016/j.tafmec.2018.09.011, URL https://www.sciencedirect.com/science/article/pii/S0167844218303173.

[31] Nadot Y, Nadot-Martin C, Kan WH, Boufadene S, Foley M, Cairney J, Proust G, Ridosz L. Predicting the fatigue life of an AlSi10Mg alloy manufactured via laser powder bed fusion by using data from computed tomography. Addit Manuf 2020;32:100899. http://dx.doi.org/10.1016/j.addma.2019.100899, URL https://www.sciencedirect.com/science/article/pii/S2214860419302842.

[32] Maskery I, Aboulkhair N, Corfield M, Tuck C, Clare A, Leach R, Wildman R, Ashcroft I, Hague R. Quantification and characterisation of porosity in selectively laser melted Al–Si10–Mg using x-ray computed tomography. Mater Charact 2016;111:193–204. http://dx.doi.org/10.1016/j.matchar.2015.12.001, URL https://www.sciencedirect.com/science/article/pii/S1044580315300711.

[33] Sanaei N, Fatemi A. Defects in additive manufactured metals and their effect on fatigue performance: A state-of-the-art review. Prog Mater Sci 2021;117:100724. http://dx.doi.org/10.1016/j.pmatsci.2020.100724, URL https://www.sciencedirect.com/science/article/pii/S0079642520300888.

[34] Marciniak Z, Branco R, Martins RF, Macek W, Rozumek D. Non-local volumetric approach to analysis defect's shape influence on specimens durability subjected to bending and torsion. Int J Fatigue 2023;167:107317. http://dx.doi.org/10.1016/j.ijfatigue.2022.107317, URL https://www.sciencedirect.com/science/article/pii/S0142112322005679.

[35] Vayssette B, Saintier N, Brugger C, El May M. Surface roughness effect of slm and ebm Ti-6Al-4V on multiaxial high cycle fatigue. Theor Appl Fract Mech 2020;108:102581. http://dx.doi.org/10.1016/j.tafmec.2020.102581, URL https://www.sciencedirect.com/science/article/pii/S0167844220301579.

[36] Bonneric M, Saintier N, El Khoukhi D, Bega J. Influence of the defect size, type, and position on the high cycle fatigue behavior of Ti-6Al-4V processed by laser powder bed fusion. Int J Fatigue 2025;193:108783. http://dx.doi.org/10.1016/j.ijfatigue.2024.108783, URL https://www.sciencedirect.com/science/article/pii/S014211232400642X.

[37] Guerchais R, Morel F, Saintier N, Robert C. Influence of the microstructure and voids on the high-cycle fatigue strength of 316L stainless steel under multiaxial loading. Fatigue Fract Eng Mater Struct 2015;38(9):1087–104. http://dx.doi.org/10.1111/ffe.12304, arXiv:https://onlinelibrary.wiley.com/doi/pdf/10.1111/ffe.12304, URL https://onlinelibrary.wiley.com/doi/abs/10.1111/ffe.12304.

[38] Crossland A. Effect of large hydrostatic pressures on the torsional fatigue strength of fan alloy steel. In: Proceedings of the international conference on fatigue of metals. 1956.

[39] Karolczuk A, Nadot Y, Dragon A. Non-local stress gradient approach for multiaxial fatigue of defective material. Comput Mater Sci 2008;44(2):464–75. http://dx.doi.org/10.1016/j.commatsci.2008.04.005, URL https://www.sciencedirect.com/science/article/pii/S0927025608002000.

[40] Morel F, Morel A, Nadot Y. Comparison between defects and micronotches in multiaxial fatigue – the size effect and the gradient effect. Int J Fatigue 2009;31(2):263–75. http://dx.doi.org/10.1016/j.ijfatigue.2008.09.005, URL https://www.sciencedirect.com/science/article/pii/S0142112308002156.

[41] Nadot Y, Billaudeau T. Multiaxial fatigue limit criterion for defective materials. Eng Fract Mech 2006;73(1):112–33. http://dx.doi.org/10.1016/j.engfracmech.2005.06.005, URL https://www.sciencedirect.com/science/article/pii/S0013794405001645.

[42] Taylor D. Geometrical effects in fatigue: a unifying theoretical model. Int J Fatigue 1999;21(5):413–20. http://dx.doi.org/10.1016/S0142-1123(99)00007-9, URL https://www.sciencedirect.com/science/article/pii/S0142112399000079.

[43] Susmel L. The theory of critical distances: a review of its applications in fatigue. Eng Fract Mech 2008;75(7):1706–24. http://dx.doi.org/10.1016/j.engfracmech.2006.12.004, Critical Distance Theories of Fracture. URL https://www.sciencedirect.com/science/article/pii/S0013794406004553.

[44] Vayssette B, et al. Numerical modelling of surface roughness effect on the fatigue behavior of Ti-6Al-4V obtained by additive manufacturing. Int J Fatigue 2019;123:180–95. http://dx.doi.org/10.1016/j.ijfatigue.2019.02.014, URL https://www.sciencedirect.com/science/article/pii/S0142112319300416.

[45] Bunge HJ. Texture analysis in materials science: mathematical methods. Butterwoth & Co; 1982.

[46] Nordmann J, Aßmus M, Altenbach H. Visualising elastic anisotropy: theoretical background and computational implementation. Contin Mech Thermodyn 2018;30:689–708. http://dx.doi.org/10.1007/s00161-018-0635-9.

[47] Beretta S, Murakami Y. Statistical analysis of defects for fatigue strength prediction and quality control of materials. Fatigue Fract Eng Mater Struct 1998;21(9):1049–65. http://dx.doi.org/10.1046/j.1460-2695.1998.00104.x, arXiv:https://onlinelibrary.wiley.com/doi/pdf/10.1046/j.1460-2695.1998.00104.x, URL https://onlinelibrary.wiley.com/doi/abs/10.1046/j.1460-2695.1998.00104.x.

[48] Fatigue strength assessment of as built AlSi10Mg manufactured by slm with different build orientations. Int J Fatigue 2020;139:105737. http://dx.doi.org/10.1016/J.IJFATIGUE.2020.105737.

[49] Zhang Y, Li X, Yuan S, Sun R, Sakai T, Lashari MI, Hamid U, Li W. High-cycle-fatigue properties of selective-laser-melted AlSi10Mg with multiple building directions. Int J Mech Sci 2022;224:107336. http://dx.doi.org/10.1016/J.IJMECSCI.2022.107336.

[50] Xu Z, Liu A, Wang X. Fatigue performance and crack propagation behavior of selective laser melted AlSi10Mg in 0°, 15°, 45° and 90° building directions. Mater Sci Eng: A 2021;812:141141. http://dx.doi.org/10.1016/J.MSEA.2021.141141.

[51] Wood P, Libura T, Kowalewski ZL, Williams G, Serjouei A. Influences of horizontal and vertical build orientations and post-fabrication processes on the fatigue behavior of stainless steel 316L produced by selective laser melting. Mater 2019;12:4203. http://dx.doi.org/10.3390/ma12244203.

[52] Yadollahi A, Shamsaei N, Thompson SM, Elwany A, Bian L. Effects of building orientation and heat treatment on fatigue behavior of selective laser melted 17-4 ph stainless steel. Int J Fatigue 2017;94:218–35. http://dx.doi.org/10.1016/J.IJFATIGUE.2016.03.014.

[53] Meneghetti G, Rigon D, Cozzi D, Waldhauser W, Dabalà M. Influence of build orientation on static and axial fatigue properties of maraging steel specimens produced by additive manufacturing. Procedia Struct Integr 2017;7:149–57. http://dx.doi.org/10.1016/J.PROSTR.2017.11.072.

[54] Sarkar S, Kumar CS, Nath AK. Effects of heat treatment and build orientations on the fatigue life of selective laser melted 15-5 ph stainless steel. Mater Sci Eng: A 2019;755:235–45. http://dx.doi.org/10.1016/J.MSEA.2019.04.003.

[55] Edwards P, Ramulu M. Fatigue performance evaluation of selective laser melted Ti–6Al–4V. Mater Sci Eng: A 2014;598:327–37. http://dx.doi.org/10.1016/J.MSEA.2014.01.041.

[56] Xu Z, Liu A, Wang X, Liu B, Guo M. Fatigue limit prediction model and fatigue crack growth mechanism for selective laser melting Ti6Al4V samples with inherent defects. Int J Fatigue 2021;143:106008. http://dx.doi.org/10.1016/J.IJFATIGUE.2020.106008.

[57] Le VD, Pessard E, Morel F, Edy F. Interpretation of the fatigue anisotropy of additively manufactured TA6V alloys via a fracture mechanics approach. Eng Fract Mech 2019;214:410–26. http://dx.doi.org/10.1016/j.engfracmech.2019.03.048.

[58] Wang Y, Su Z. Effect of micro-defects on fatigue lifetime of additive manufactured 316L stainless steel under multiaxial loading. Theor Appl Fract Mech 2021;111:102849. http://dx.doi.org/10.1016/j.tafmec.2020.102849, URL https://www.sciencedirect.com/science/article/pii/S0167844220304250.